RESEARCH ARTICLE

Ictal wavefront propagation in slices and simulations with conductance-based refractory density model

Anton V. Chizhov[1,2]*, **Dmitry V. Amakhin**[1], **Elena Yu. Smirnova**[1,2,3], **Aleksey V. Zaitsev**[1]

1 Laboratory of Molecular Mechanisms of Neural Interactions, Sechenov Institute of Evolutionary Physiology and Biochemistry of the Russian Academy of Sciences, Saint Petersburg, Russia, 2 Computational Physics Laboratory, Ioffe Institute, Saint Petersburg, Russia, 3 Institute of Experimental Medicine, Almazov National Medical Research Centre, Saint Petersburg, Russia

* anton.chizhov@mail.ioffe.ru

Abstract

The mechanisms determining ictal discharge (ID) propagation are still not clear. In the present study, we aimed to examine these mechanisms in animal and mathematical models of epileptiform activity. Using double-patch and extracellular potassium ion concentration recordings in rat hippocampal-cortical slices, we observed that IDs moved at a speed of about 1 mm/s or less. The mechanisms of such slow propagation have been studied with a mathematical, conductance-based refractory density (CBRD) model that describes the GABA- and glutamatergic neuronal populations' interactions and ion dynamics in brain tissue. The modeling study reveals two main factors triggerring IDs: (i) increased interneuronal activity leading to chloride ion accumulation and a consequent depolarizing GABAergic effect and (ii) the elevation of extracellular potassium ion concentration. The local synaptic transmission followed by local potassium ion extrusion and GABA receptor-mediated chloride ion accumulation underlies the ID wavefront's propagation. In contrast, potassium ion diffusion in the extracellular space is slower and does not affect ID's speed. The short discharges, constituting the ID, propagate much faster than the ID front. The accumulation of sodium ions inside neurons due to their hyperactivity and glutamatergic currents boosts the Na^+/K^+ pump, which terminates the ID. Knowledge of the mechanism of ID generation and propagation contributes to the development of new treatments against epilepsy.

Author summary

During an epileptic seizure, neuronal excitation spreads across the brain tissue and is accompanied by significant changes in ionic concentrations. Ictal discharge front spreads at low speeds, less than 1 mm/s. Mechanisms underlying this phenomenon are not yet well understood. We study these mechanisms using electrophysiological recordings in brain slices and computer simulations. Our detailed biophysical model describing neuronal populations' interaction, spatial propagation, and ionic dynamics reproduces the

generation and propagation of spontaneously repeating ictal discharges. The simulations are consistent with our recordings of the electrical activity and the extracellular potassium ion concentration. We distinguished between the two alternative mechanisms of the ictal wavefront propagation: (i) the diffusion of potassium ions released from excited neurons, which depolarizes distant neurons and thus supports excitation, and (ii) the axonal spread of excitation followed by the local extracellular potassium ion accumulation that supports the excitation. Our simulations provide evidence in favor of the latter mechanism. Our experiment-based modeling contributes to a mathematical description of brain tissue functioning and potentially contributes to developing new treatments against epilepsy.

Introduction

The exact nature of spatiotemporal dynamics of brain activity during seizures is of great importance. However, the mechanisms of epileptic discharge propagation are not yet well understood. Epileptic activity in the brain is divided into several forms, including long-lasting (with a duration of tens of seconds) ictal discharges (IDs) and different types of short-lasting discharges (SDs) of less than one or a few seconds [1]. Several forms of SDs are distinguished: (i) predominantly, GABAergic interictal discharges (IIDs) emerging between IDs; (ii) IID-like preictal discharges (PIDs) that may take place just before an ID; and (iii) GABA-glutamatergic late short discharges (LSDs) that constitute either an ID in its late phase (known as intraictal bursts in [2]) or continuously repeating in status epilepticus. These discharges propagate through the brain tissue at different speeds. The typical speed of SD propagation is about tens of millimeters per second [2–6]. ID propagation is slower; the rate is less than 1 mm/s in the cerebral cortex of patients [7–9] and animals *in vivo* [10,11] and *in vitro* [2,3,12–14]. The difference in speeds of IDs and SDs suggests different mechanisms of propagation. The consensus among previous studies is that SD generation and propagation mechanisms are not related to ion dynamics, which implies only neuronal excitation and synaptic interactions [6,15–17]. In contrast, the generation of IDs critically depends on ion dynamics [18–21], which is often mistakenly omitted in many other modeling studies. Whether the contribution of the ion dynamics into the ID propagation is direct—due to ion diffusion—or indirect—as a consequence of neuronal excitation—is still debated [22].

A slowly propagating wave of ID is accompanied by a wave of increasing extracellular potassium ion concentration [1]. However, it is still unclear whether ictal activity causes an increase in potassium ion concentration or, conversely, diffusion of potassium ions from sites of high concentration causes ictal activity. Therefore, at least two alternative mechanisms of ID propagation have been suggested: (i) synaptic transmission between neurons, including spike propagation through axons and passive conduction of postsynaptic signals through dendritic neuronal branches [23,24]; (ii) the diffusion of potassium ions, resulting from substantial transient increases in extracellular potassium ion concentrations that are observed during IDs [1,25,26].

Recently, using the proposed spatially distributed extension of the simple model of IDs and SDs Epileptor-2 [27], we compared the impacts of synaptic transmission and potassium ion diffusion in 2-D simulations [28]. We showed that potassium ion diffusion can contribute to ictal discharge propagation; however, it leads to an ID propagation speed of much less than 0.1 mm/s. Instead, the synaptic connectivity-based mechanism provides a speed comparable to experimental data. However, due to the reductions made in the Epileptor-2, it cannot be compared to electrophysiological experiments in detail and, in particular, does not exclude any indirect effects of potassium ion diffusion. Therefore, here we use our detailed mathematical

model based on the conductance-based refractory density (CBRD) approach and extend it to the 1-D spatially distributed case. We simulate the propagation of repeating IDs and compare the simulations with our recordings of neuronal electrical activity and extracellular potassium ion concentration in two points of the entorhinal cortex (EC) at a distance of 2 mm in rat brain slices in the 4-aminopyridine model. The obtained results indicate that the accumulation of extracellular potassium ions due to synaptic activity but not potassium ion diffusion promotes ID propagation.

Results

Experimental observations of ictal front propagation

We induced the epileptiform activity in rat brain slices and performed the simultaneous recordings of the synaptic currents and the $[K^+]_o$ fluctuations (Fig 1A). The epileptiform activity in the implemented *in vitro* model was described in detail in our previous works [21,29,30]. Briefly, two main types of epileptiform discharges were observed: GABA-mediated IIDs (marked with blue arrows in Fig 1A) and subsequent IDs (marked with brown arrows in Fig 1A), which are mediated by both GABA and glutamate. IIDs had a duration of about 1 s and, in some cases, transitioned to the IDs, which had the duration of 25–100 s and emerged every 5–10 min. The IIDs, which directly preceded IDs, will be referred to as preictal discharges (PIDs).

During each ID, we observed a substantial increase in extracellular potassium ion concentration (Fig 1B). In most cases, the rise in potassium ion concentration came in two stages (Fig 1C). The first minor rise of $[K^+]_o$ corresponded to the GABA-mediated PID. The second more significant rise of $[K^+]_o$ occurred during the tonic phase of ID and coincided with the emergence of glutamate-mediated currents.

$[K^+]_o$ peaked during the tonic phase of the ID (the average peak $[K^+]_o$ was 9.5 ± 0.3 mM, $n = 27$ IDs from nine slices), after which it gradually decreased. The late-stage clonic discharges produced transient increases of $[K^+]_o$ (Fig 1D), which did not change the overall decreasing trend. In half of the IDs included in the analysis, the K^+ concentration transiently decreased below the level observed before the ID.

Next, we investigated the ID propagation in the neocortex performing simultaneous whole-cell patch-clamp recordings in the entorhinal (ERC) and perirhinal cortices (PRC) at a distance of 2 mm between the recording electrodes. In 85% of cases included in the analysis (with the delays longer than 1 s), we detected the IDs in both cortical areas with a delay in the initiation of several seconds (Fig 2), thus obtaining a wide variety of speed values of the order of magnitude of tenths of a millimeter per second. The delay between the IDs was observed in both voltage-clamp and current-clamp modes (Fig 2A and 2B, respectively). Some IDs (15%) failed to propagate and could be detected in only one cortical area (Fig 2C).

As the shape of the K^+ transients during each ID is relatively standard with its rising phase being related to the recruitment of glutamatergic neurons into the activity, we measured the time delay between rises of K^+ transients in the ERC and PRC to estimate the propagation speed (Fig 3). The half-maximal $[K^+]_o$ was used as a reference point to measure the delay between the events (Fig 3B), thus ignoring the initial weak component, presumably determined by the potassium ion outflux from synapses activated by long-range connections. The delays between K^+ transients were comparable to those observed using the patch-clamp method, and the median speed was estimated to be 0.52 mm/s (IQR: 0.34–0.81, $n = 17$ pairs of IDs from eight slices). No significant difference between propagation speed from ERC to PRC and from PRC to ERC was detected ($p = 0.42$, Mann–Whitney U test). The recordings, where the ID-related K^+ transient failed to propagate from one cortical area to another, were not used for speed estimations (Fig 3C). Concluding the presentation of experimental results, we
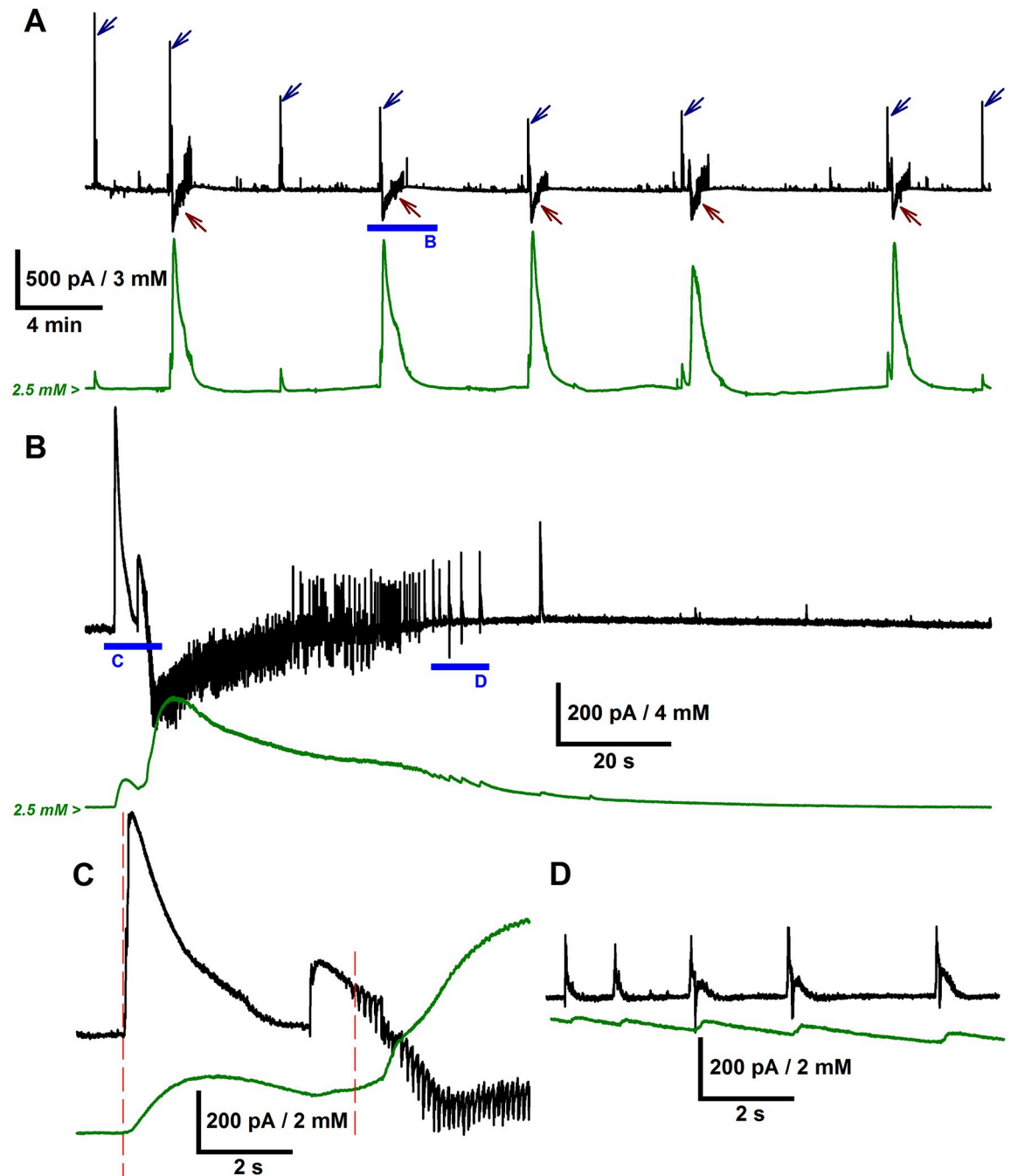
Fig 1. A neuronal and ionic dynamics correlation is revealed with the simultaneous whole-cell patch-clamp and extracellular potassium ion concentration recordings during epileptiform activity in rat ERC. (A) The representative recordings of synaptic currents in the voltage-clamp mode (black trace) and extracellular potassium ion concentration (green trace). V_{hold} = −27 mV, which is between the reversal potentials of $GABA_A$ and glutamate receptor-mediated currents. Outward GABA-mediated synaptic current corresponds to IIDs and PIDs and is marked with blue arrows. Inward, predominantly glutamate-mediated currents correspond to IDs and are marked with brown arrows. Note that all IIDs, PIDs, and IDs induce K^+ transients. The blue bar marks a fragment of the recording, which contains PID and ID and is extended in (B). (B) K^+ transient has a two-stage rise, corresponding to PID and ID initiation, respectively. The ID initiation phase is extended in (C). (C) Red dashed lines indicate the start of the PID and the emergence of glutamate-mediated components at the beginning of the ID. The late stage of the ID consisted of short discharges, which are extended in (D). (D) Each of these late-stage discharges produces a transient increase of $[K^+]_o$.
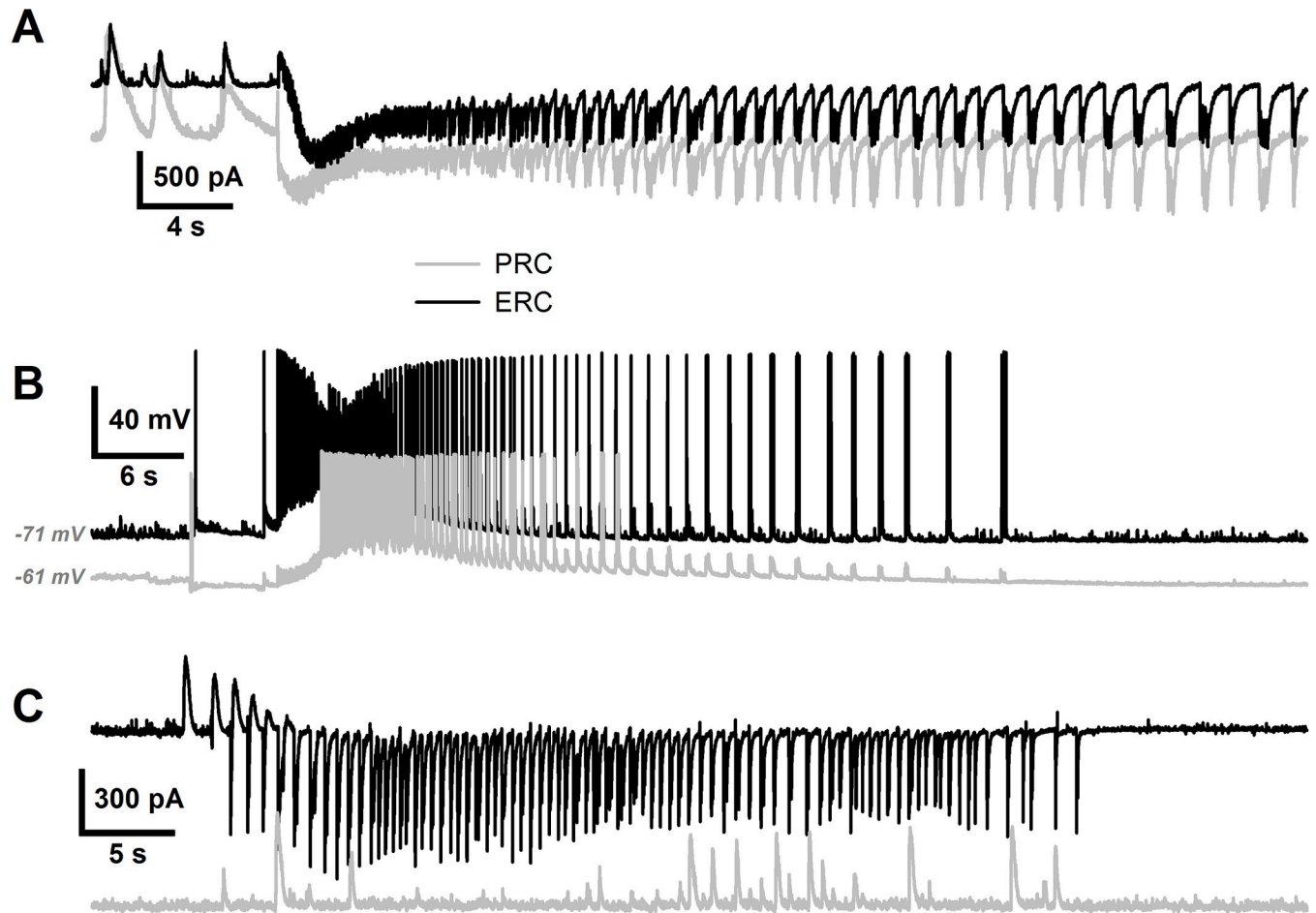
Fig 2. The representative simultaneous whole-cell patch-clamp recordings of IDs in the ERC and PRC. (A) Dual voltage-clamp recordings (V_{hold} = −27 mV) of synaptic activity during IDs at a distance of 2 mm. A delay between the tonic phases of the IDs is observed. (B) Dual current-clamp recordings of membrane voltage during IDs. Note the delay between the IDs, which is comparable to the one in A. (C) A representative dual voltage-clamp recording illustrating the absence of ID propagation from one cortical area to another in the slice.

point out that our experiments and similar previous studies mentioned in the Introduction reveal a challenging task to explain the mechanism of slow propagation of ID wavefront with the speed of the order of magnitude of tenths of a millimeter per second.

Simulation of the ictal front wave

Aiming to reproduce and explain the experimentally observed epileptiform activity, we have constructed a mathematical model (see the Methods section) that describes the main physiological mechanisms underlying interactions between neuronal populations in the cortical tissue. Below, we begin with the description of the simulated phenomenon, then pass to the mechanisms of ID generation and end up with the analysis of ID propagation.

Phenomenon

We simulated neuronal activity in a spatially extended cortical domain (Fig 4A, yellow domain), thus obtaining the spatial-temporal distributions of the main variable, the membrane voltage, ionic concentrations, etc. (Fig 4B–4D) and the signals from one (Fig 5) or two spatially remote sites S1 and S2 (Figs 4E and 5C). The model reproduces the spontaneous generation of
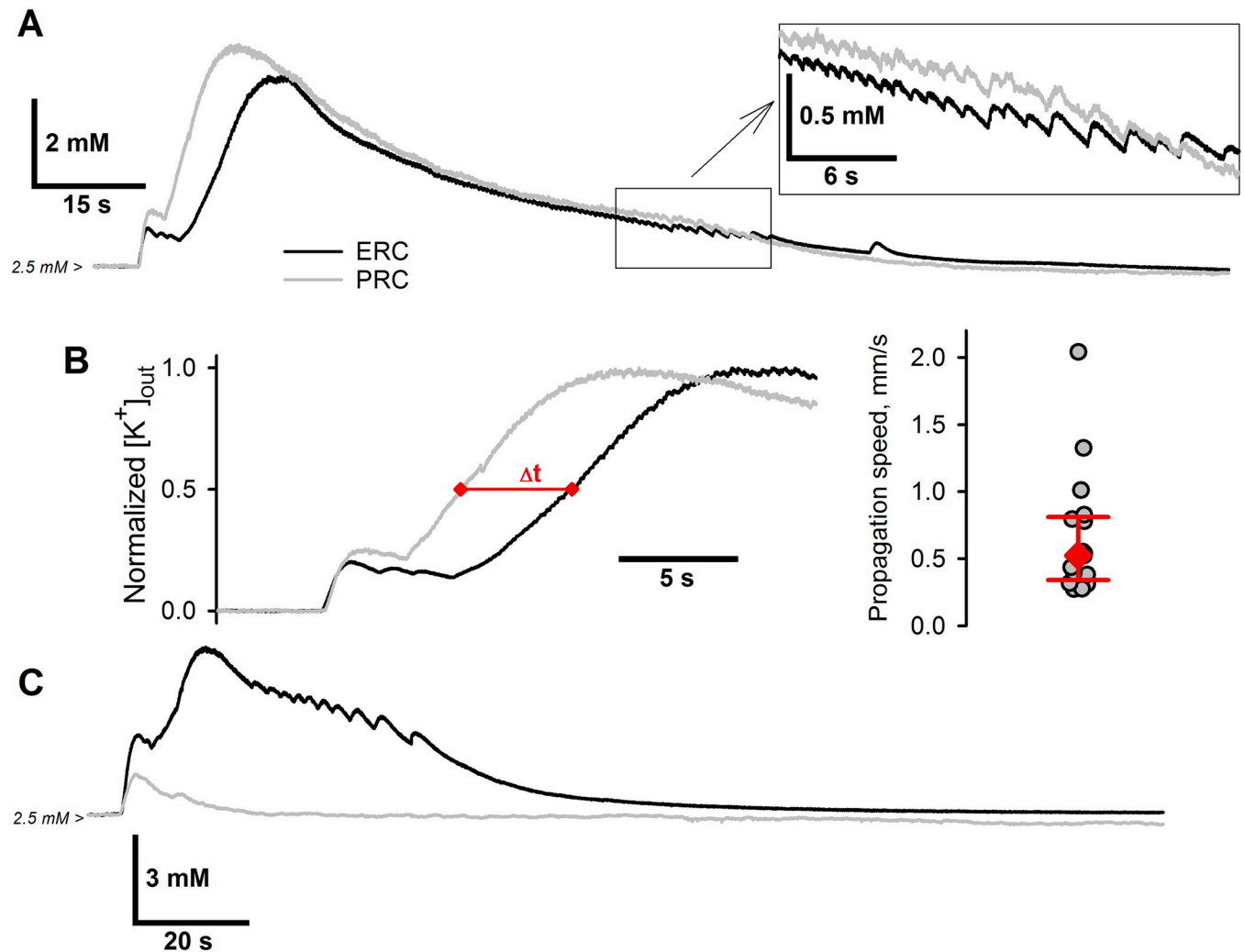
Fig 3. Experimental estimations of the ID propagation speed. (A) The representative paired recordings of $[K^+]_o$ during the IDs at a 2-mm distance between the electrodes. Note the substantial delay of the $[K^+]_o$ rise in PRC relative to ERC. A fragment corresponding to the late-stage discharges is extended in the box. Late-stage discharges produce the almost synchronous K^+ transients. (B) Left panel: measurement of the delay between normalized K^+ transients. The time lag between the $[K^+]_o$ rises was measured at a half peak value of $[K^+]_o$. Right panel: the estimation of the ID propagation speed. The red diamond indicates the median value; error bars indicate 75th and 25th percentiles. (C) A representative example of the absence of ID-related K^+ transient propagation from one cortical area to another in the slice.

https://doi.org/10.1371/journal.pcbi.1009782.g003

repeating IDs and their spread. Similar to the experimental data, the model generates IDs every few minutes (mean ID frequency was 0.59 s^{-1}; Fig 4F) that last for tens of seconds (Figs 4B–4E and 5). At the beginning of each ID, the outward GABAergic current predominates, and the simulated current at the holding voltage of −27 mV exposes short positive, i.e., GABAergic, bursts (Fig 4E, next to bottom; blue arrows in Fig 5A; compare to the experiment in Fig 1A). Then, the inward glutamatergic current prevails, exposing long-lasting negative, i.e., glutamatergic, components (Fig 4E, next to bottom; brown arrows in Fig 5A), similar to what is observed in the experiment (Figs 1 and 2A). These GABAergic and glutamatergic components constitute an ID. Each ID is characterized by the rapid increase in the concentration of the extracellular potassium ions, which peaked in simulations up to 14 mM (Fig 4F). The traces of $[K^+]_o$ at the sites S1 and S2, shown in Fig 4E, have similar shapes. The rapid growth of $[K^+]_o$ is delayed at one of the electrodes. It is in contrast to such traces obtained in the model
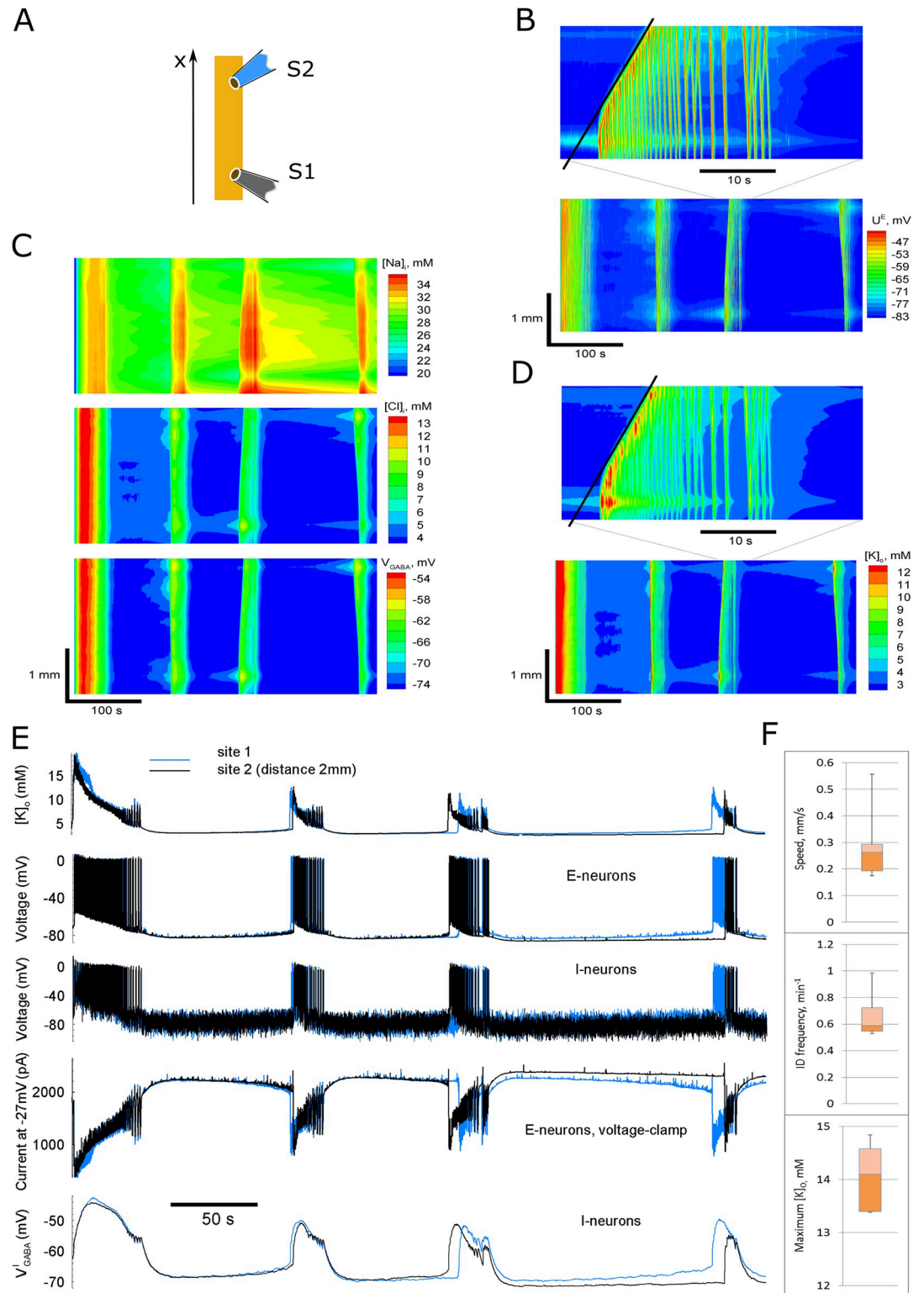
Fig 4. Ictal discharges simulated in the 1-D model. (A) Schematic diagram of the computational domain and the locations of "electrodes" S1 and S2. (B–D) Space-time plots for: (B) the mean membrane potential of E-neurons, (C) the intracellular sodium and chloride ion concentrations, and the GABA reversal potential, (D) the extracellular potassium ion concentration. (E) signals from two sites, S2 (black) and S1 (blue): the extracellular potassium ion concentration, the membrane potential of two remote representative neurons, the current calculated at the "holding" voltage -27mV, and the reversal potential of

GABA-A receptors on interneurons. (F) Statistics of the estimated characteristics of the activity, obtained from simulations with the different realizations of noise (3 discharges in 5 simulations, i.e., n = 15): the speed of the wavefronts, the interdischarge frequency, and the maximum value of the extracellular potassium ion concentration reached during IDs. The slope of the black lines in B and D determines the speed of the ictal wavefront. The arrows in bottom panel B point to the ID origination sites.

that takes into account long-range (all-to-all) connections, which reveal a rather simultaneous initiation with weak components (Fig 5C), similar to that in experiments (Fig 3). As discussed below in the paragraph of the Results section "ID propagation in the networks with additional all-to-all connections," the long-range connections do not affect the bulk of IDs, and thus they are omitted in most of the simulations.

Mechanism of ID generation

We observe that in our conditions, interneurons do not inhibit but instead stimulate the pyramidal cells, whose activity then constitutes each new ID. Between IDs, the interictal and preictal GABAergic components seen as positive current events in Fig 5A are determined by spiking of the I-neurons, characterized by their firing rate shown in Fig 6E (see also the positive currents in Fig 7B and the I-neurons' firing rate in Fig 7J). The interneurons start to fire spontaneously before the ID (see small initial events in the firing rate trace for the I-population in Figs 6E and 7J). The I-neurons' initial firing is determined by the noise that mimics spontaneous synaptic activity, observed in the experiment and caused by increased synaptic transmitter release after 4-aminopyridine application. The enhanced I-neurons' firing increases the frequency of IPSCs (positive current events between IDs in Fig 5A and orange curve for the GABAergic current in Fig 6D).

The chloride movement into and out of cells is described as a sum of the passive conductive flux [31] and fluxes mediated by three proteins: the two cation-chloride-transporters, KCC2 and NKCC1, and the GABA$_A$ receptors (see I^I_{GABA} in Fig 6D). Their effect leads to a gradual accumulation of chloride ions inside neurons. The GABA reversal potential (Fig 4E, bottom, and Fig 6F) and the leak reversal potential (Fig 6F) increase due to chloride ion accumulation inside the cells. At every GABA-mediated event, the membrane potential tends to approach the GABA reversal potential, which is always above the chloride ion reversal potential (Fig 6F) because of the bicarbonate ion permeability of GABA$_A$ receptors. In the case of membrane potential being above the chloride ion reversal potential, the activation of GABA$_A$ receptors increases the chloride ion entry into the neurons, even in the absence of depolarization by glutamatergic currents.

The KCC2 transporters diminish the difference between the reversal potentials for chloride and potassium ions. Thus, the elevation of $[Cl^-]_i$ results in the elevation of $[K^+]_o$ and depolarization. The gradual depolarization of neuronal membranes and the depolarizing effect of spontaneous GABA- and glutamate-mediated events lead to excitation and synchronization of some I-neurons. The frequency of short bursts of I-cell excitation increases (see more significant events in the firing rate trace for the I-population in Fig 6E after $t = 180$ s).

The GABAergic activity leads to chloride ion accumulation in E-neurons (see the intracellular chloride ion concentration in Fig 6G), raising the reversal potential of GABA$_A$ receptor-mediated current and membrane potential. Therefore, I-neurons excite E-neurons, triggering glutamatergic events (see the E-population firing rate in Fig 6E and Fig 7I).

Glutamatergic excitation and elevation of $[K^+]_o$ act as positive feedback, thus maintaining the neural network's overexcitation. In opposition to glutamatergic drive, the synaptic resource, i.e., the pool of synaptic vesicles ready to release, is depleted (Fig 7C) and interrupts firing, thus splitting ID into a series of bursts, LSDs (Fig 7E).
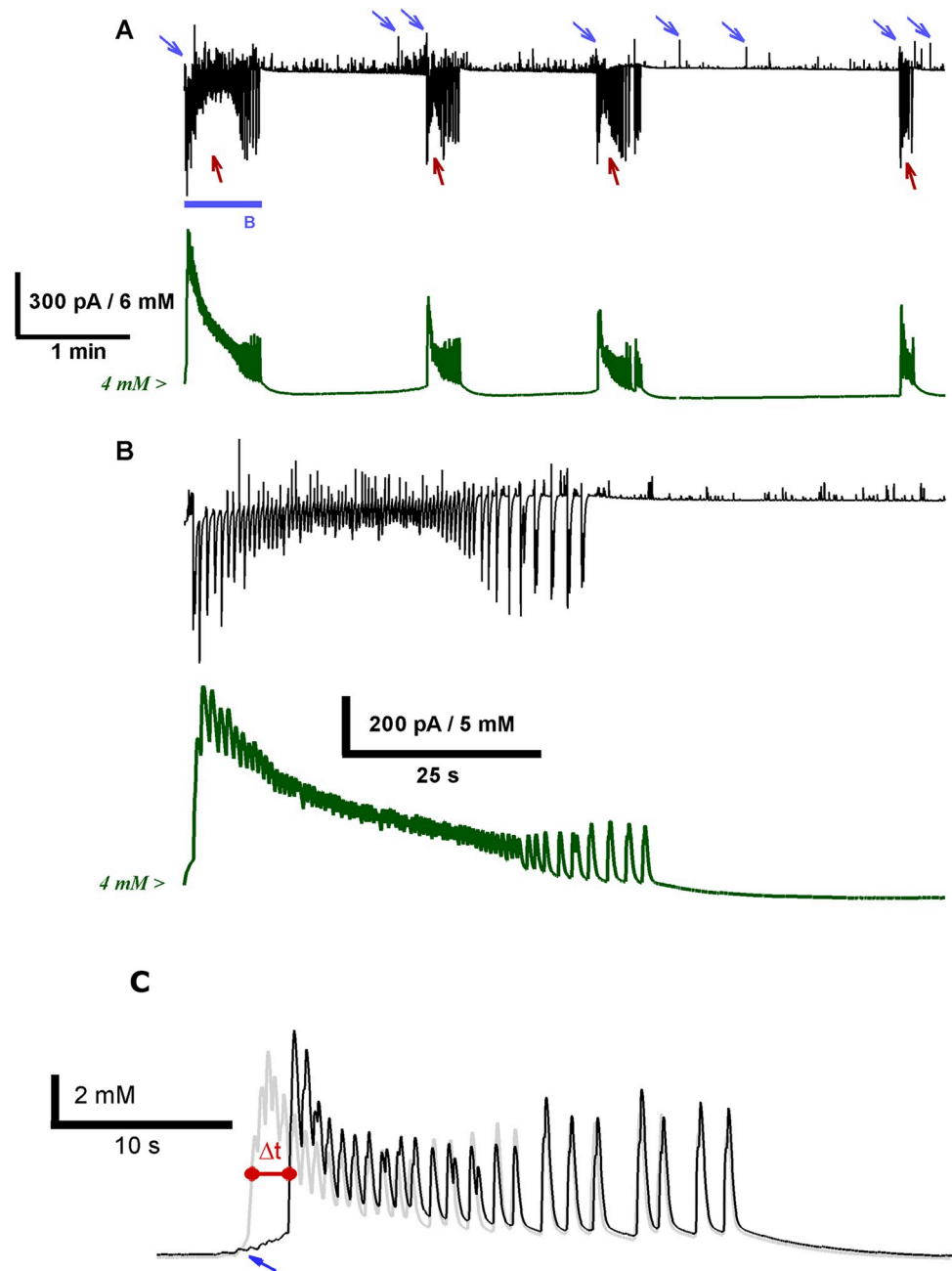
Fig 5. Neuronal and ionic dynamics during ID generation in a simulation are similar to experimental recordings from Figs 1 and 3. (A and B) The signals are the current calculated in the voltage-clamp mode with blocked potassium ion currents (top traces in A and B) and $[K^+]_o$ (bottom). Blue arrows mark the interictal or preictal GABAergic discharges. Red arrows mark the glutamatergic components of IDs. (C) the traces of $[K]_o$ at two sites S1 and S2, located at one-fourth of the length from both ends of the simulated "slice" (Fig 4A), in the model that takes into account long-range (all-to-all) connections. The blue arrow marks the initiation of potassium response simultaneously at the two sites. The red notch shows the delay (about 2ms) used to estimate the propagation speed (0.6mm/s for the distance between the electrodes 1.2mm).

Sodium and potassium ion currents through voltage-gated and glutamatergic channels elevate $[K^+]_o$ and $[Na^+]_i^E$ (Fig 6A and 6B). High $[Na^+]_i$ activates the Na^+/K^+ pump. The pump provides a hyperpolarizing current and recovers the potassium transmembrane gradient, thus
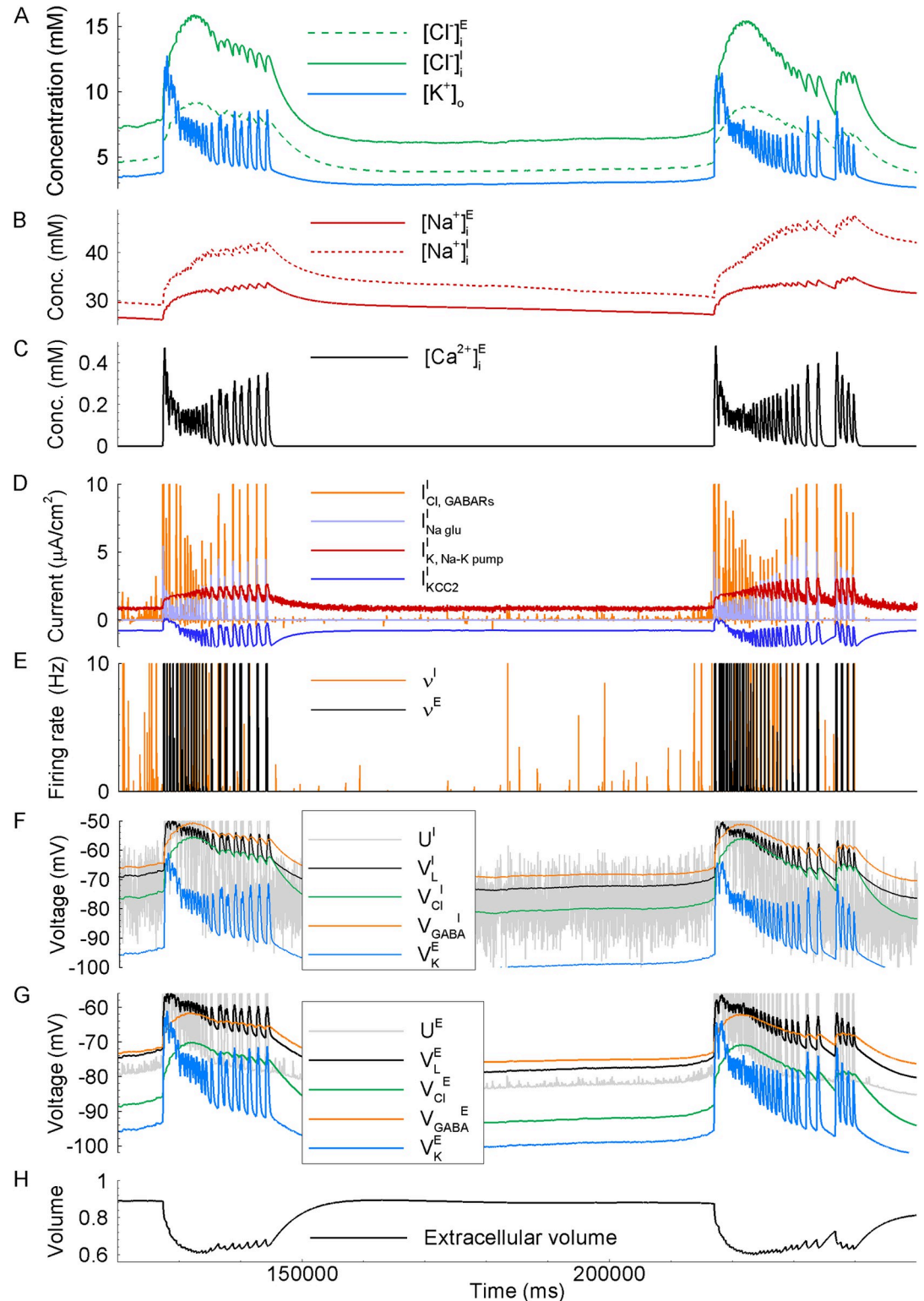
Fig 6. Interneuronal activity triggers IDs in simulation, site S1. For the second and third IDs (as in [Fig 4](#)), the following signals are shown (top to bottom): (A) the extracellular potassium and intracellular chloride ion concentrations; (B) the intracellular sodium ion concentrations; (C) the intracellular calcium concentration in E-cells; (D) the GABA-mediated chloride ion current, the glutamatergic sodium ion current, the potassium ion current via the Na$^+$/K$^+$ pump, and the potassium ion current via the KCC2 cotransporters for I-cells; (E) the firing rates of the E- and I-cells; (F and G) the membrane

potential and the reversal potentials of the total leak, chloride ion and GABAergic currents, and the reversal potential of the potassium ion current, for the *E-* and *I*-cells, respectively; (H) the ECS volume.

diminishing the positive feedback. It results in the termination of ID. The $[Na^+]_i$ returns to its normal level with some delay, and the pump over-decreases $[K^+]_o$, which results in a pause in neuronal firing and determines the interval between IDs.

This mechanism of ID generation is consistent with previous studies [21,32,33]. In particular, the dynamics of the neuronal membrane potential and the ionic concentrations is similar to the "best approximations based on the available literature," presented in [32], as seen from a comparison of the panels of Fig 8. $[K^+]_o$ peaks at the initial phase of ID with an undershoot accompanying the interval between IDs, as in Fig 1A. $[Na^+]^E_i$ is likely to peak at the end of the ID [18]. $[Cl^-]^E_i$ reflects the recordings from [33,34]. The aforementioned activation of the Na^+/K^+ pump explains the earlier peak of $[K^+]_o$, the later peak of $[Na^+]^E_i$ and the undershoot of $[K^+]_o$.

ID propagation

In simulations, as in our experiments, different IDs emerge in distinct parts of the slice. For the simulation shown in Fig 4, the sites of ID origination are marked by arrows in bottom panel B. For instance, the last two IDs (Fig 4B) appear on opposite sides of the "slice." Except for the duration, the signals recorded in spatially remote sites are similar (Figs 4E and 7). The ID at the leading site lasts longer, such that the ID ceases almost simultaneously at different places, as often observed in experiments [2,35]. At the onset of ID, $[K^+]_o$ and the membrane potential in all types of neurons rise more gradually in the site-follower (Fig 7, blue curves) than in the leading site (black curves). In the later phase of ID, the LSDs appeared almost simultaneously in both sites. Any PIDs that were sometimes observed in the experiments were not present in the simulations.

While some of the IDs appear almost simultaneously in different locations, i.e., their apparent speed is large, the others propagate with limited speed. Our study focuses on the propagation of IDs at a minimum velocity. A few-second delay is observed between some of the IDs recorded at a 2-mm distance (Fig 4E). For instance, the delay is about 5 s for the third ID shown in Fig 7A. Respectively, the ID wavefront speed is estimated to be 0.4 mm/s, which is a typical minimal speed among different IDs in different realizations of simulations with the fixed control settings (mean value 0.26 mm/s; Figs 7F and 9H). This value within an order of magnitude is consistent with our experimental estimates and the experimental data from other laboratories [3,10,11].

ID propagation in conditions of no potassium ion diffusion

Our mathematical model includes two mechanisms that may contribute to ID propagation: (i) the diffusion of potassium ions through extracellular space, described by Eq 27 and (ii) the propagation of action potentials through axons, followed by the transmission through synapses and propagation of postsynaptic signals by dendrites, described by the connection profile, Eq 33, with the synaptic conductance equations, Eqs 14–18. To separate the effects of the two mechanisms, we blocked potassium ion diffusion (last term in Eq 27). Still, we observed repeating ictal discharges (Fig 9B) with a pattern that differed slightly but was qualitatively similar to the control case (compare Fig 9B to 9A). The time difference in the ID onsets was similar to that in the control case, suggesting that the ID propagation speed was about 1 mm/s or less. This evidence indicates that the diffusion of potassium ions is insignificant. It indicates
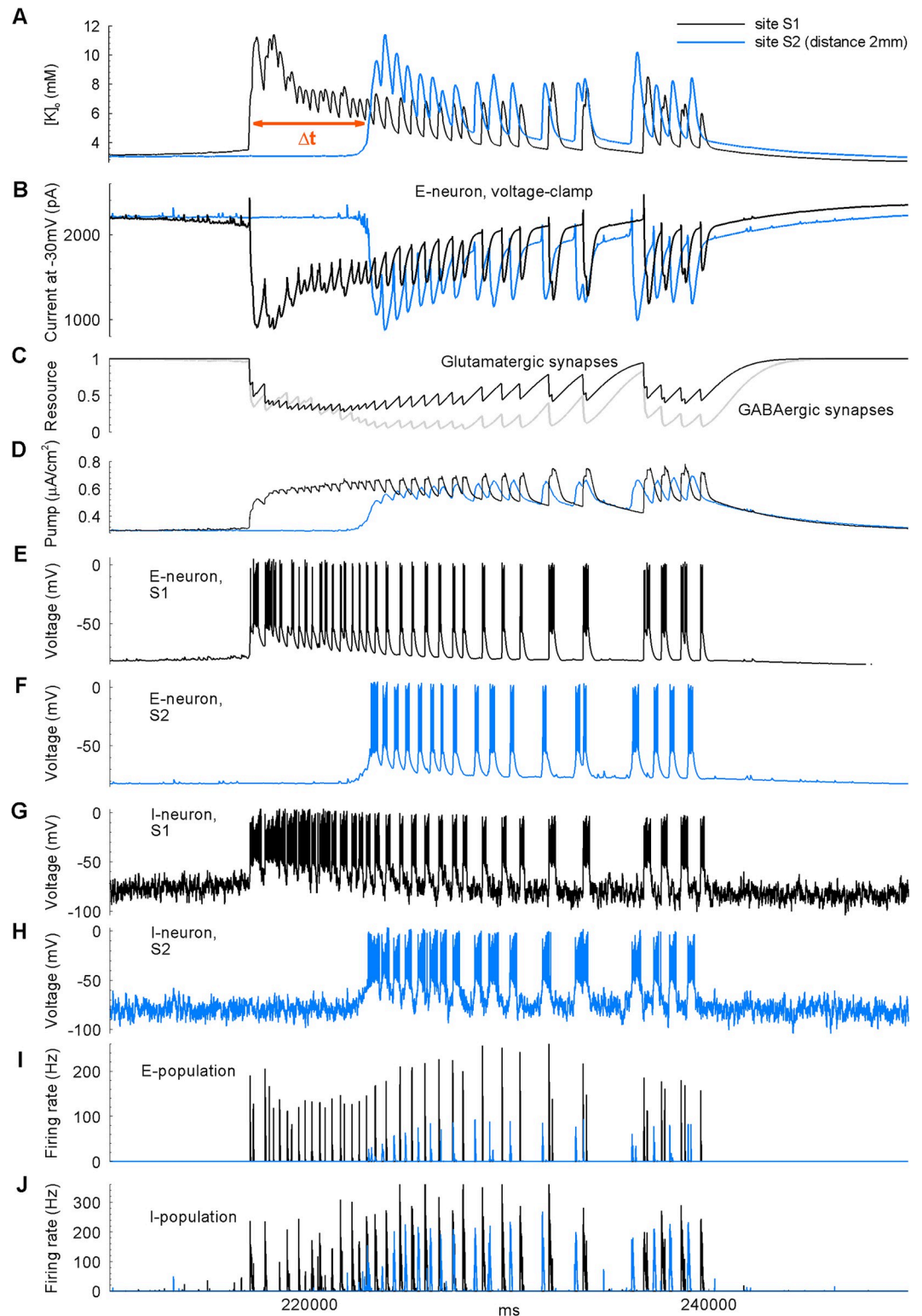
Fig 7. Single ID simulated in the 1-D model. Black–site S1, blue–S2. Red notches mark the interval between IDs registered at the sites S1 and S2.
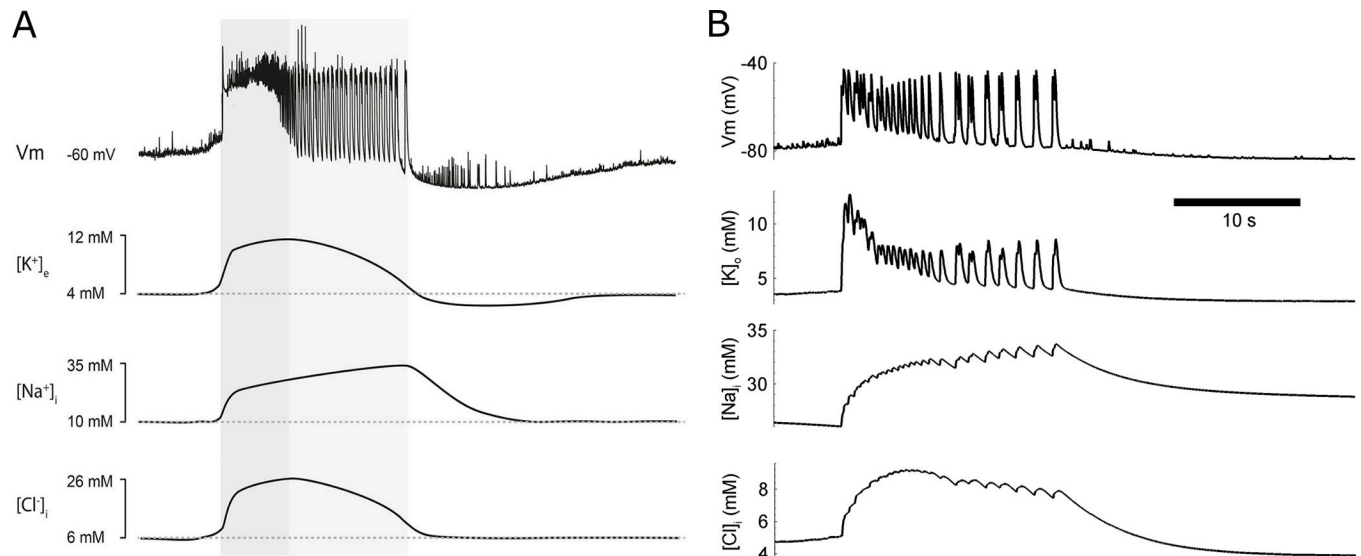
Fig 8. Comparison of simulation with experiment. Neuronal membrane potential and ionic concentration dynamics during a single ID. (A) Experimental "best approximations" based on the available literature, adopted from [32]. The dark and light gray areas mark the tonic and phasic phases of ID. (B) Simulation as in Figs 5–7.

that the primary mechanism of ID propagation is based mainly on spatially distributed synaptic connections.

ID propagation in the networks with non-spreading connections

Next, we tested whether artificial elimination of synaptic connections' spatial spread has a decisive effect on discharge propagation. For this purpose, we changed the characteristic length of the Gaussian profile of the strengths of the connections λ to 0 in Eq 33, thus obtaining $\varphi_{i,j}(t,x) = v^i(t,x)$, i.e., the presynaptic firing rate $\varphi_{i,j}(t,x)$ at any position x for the population j is now determined by the firing activity $v^i(t,x)$ of the corresponding neuronal population i in the same position x, no longer integrating the firing rates from nearby or remote neurons. Simulation has shown a dramatic change in the activity pattern (Fig 9C). Still, at every position x at the same time interval 400 s, we observe four or five IDs; however, the discharges are not so synchronized as in the previous simulations. However, there are aligned patterns with a slope corresponding to the extremely slow propagation (between 0.1–0.01 mm/s). These effects seem similar to the spreading depression, which may spread through K diffusion, with almost no synaptic effects.

The dramatic difference between activity patterns in Figs 8A and 9 confirms the primary role of synaptic connections and their spread in wavefront propagation.

ID propagation in conditions of excessive potassium ion diffusion. Since the potassium ion diffusion may hypothetically provide the propagation of discharges, in the conditions of eliminated spatial spread of synaptic connections, we increased the diffusion coefficient 1000 times (390 instead of 0.39 μm^2/ms) but maintaining $\lambda \to 0$. The simulation gave the spatially structured pattern shown in Fig 9E. It is consistent with the modeling results by Martinet et al. (2017) [22], where the diffusion coefficient was set to be 10^5 μm^2/ms. Nevertheless, such a significant discrepancy in the numbers argues against the potassium ion hypothesis.

ID propagation in the networks with long connections. If the potassium ion diffusion's role is negligible, then the speed of the ID wavefront must depend on the spatial parameter λ in the governing equations. We increased λ fivefold and obtained the pattern with fast-propagating
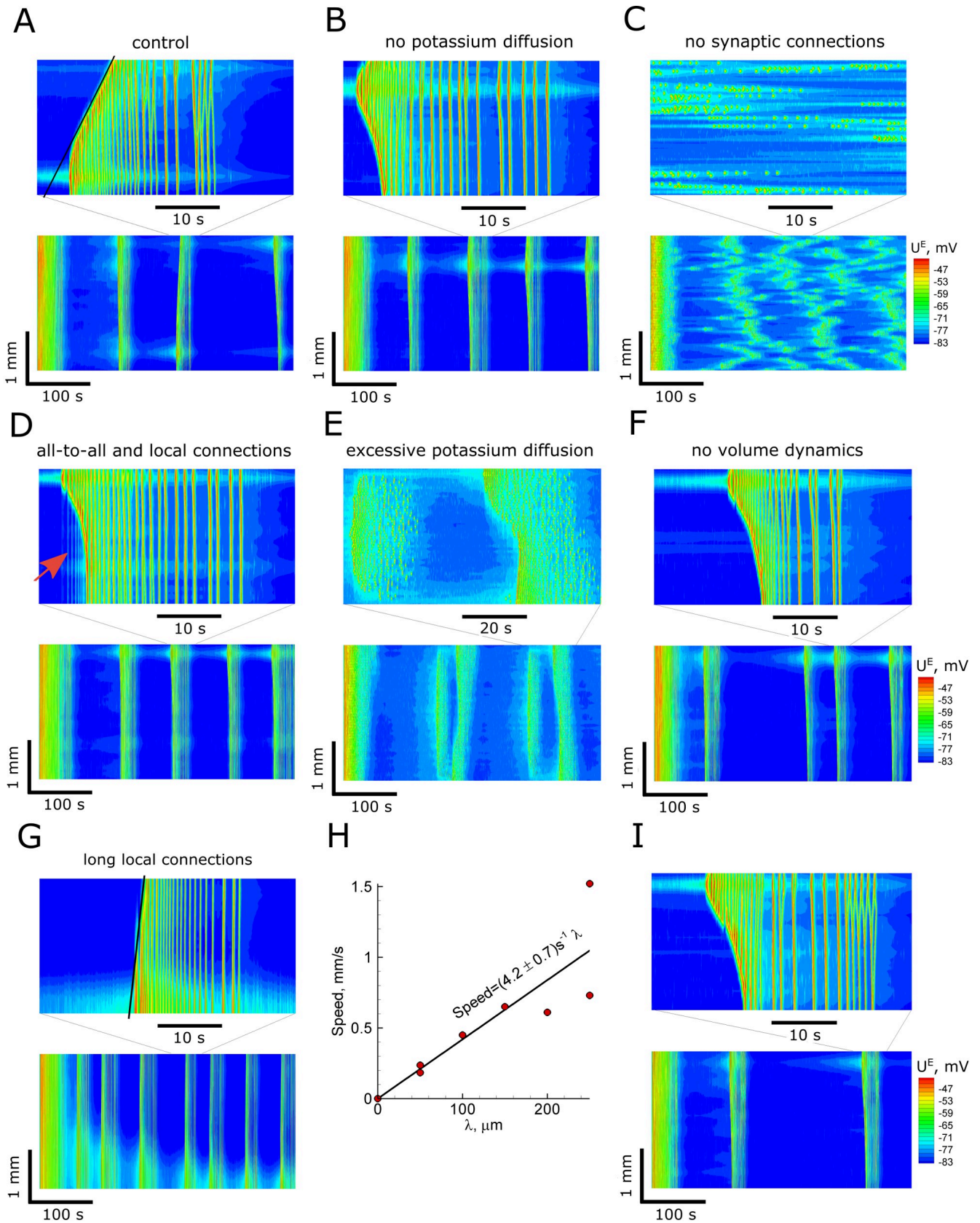
Fig 9. Ictal discharges simulated in the 1-D model with different spatial propagation mechanisms. (A) The control case is as in Fig 4D. (B) Blockade of extracellular potassium ion diffusion does not change the generation of the IDs and their speed. (C) Eliminated spatial spread of synaptic connections results in uncorrelated spatial activity. (D) Preictal bursts emerge in the presence of spatially homogeneous, all-to-all connections. (E) Non-spreading synaptic

connections and an artificially increased potassium diffusion coefficient (D_{1d} = 390 instead of $0.39 \mu m^2/ms$) result in propagating IDs. (F) Blockade of the volume dynamics increases the irregularity of the ID intervals. (G) The speed of the ID increases with the increased length of local connections (λ = $250\mu m$ instead of $50\mu m$). (H) The ID speed is proportional to the length of the connections. (I) The glial buffer increases the intervals between IDs.

IDs (Fig 9G). The speed was 1.1 mm/s instead of 0.28 mm/s in the control case (Fig 9A) or 0.35 mm/s in a lack of potassium ion diffusion and short connections (Fig 9B). Hence, the connection length is the major factor that determines the speed of IDs. Neglecting potassium ion diffusion, the length of connections is the only spatial scale in the model, which enters through Eq 33. Hence the ID speed is just proportional to λ. Estimating the speed of the slowest waves in simulations with different values of λ and different realizations of noise (Fig 9H), we obtained the coefficient of the proportionality to be 4.2 ± 0.7 s^{-1}.

ID propagation in the networks with additional all-to-all connections

In the previous simulations, we considered Gaussian-like profiles of spatially-extended connections without long-range connections, which may affect ID propagation. We also suggest that the effect of long-range connections explains the appearance of PIDs observed in the experiments but missed in the simulations mentioned above. To test these hypotheses, we added homogeneous global connections to the Gaussian profile. To this end, a fraction of the presynaptic rate (0.2) was set to be proportional to the firing rate averaged across the entire domain. As a result, the activity pattern remained approximately the same as in the control case (Fig 9D), but weak pre-ictal bursts became evident (see the arrow in Fig 9D). The PIDs are accompanied by the weak raise of $[K]_o$, initiated almost immediately in the whole "slice," as seen from the traces at two sites (Fig 5C). The weak $[K]_o$ growth is determined by the potassium outflux from the synapses activated by the long-range connections. Since the fraction of these connections is small, the weak raise of $[K]_o$ does not affect the bulk of ID. Thus, the long-range connections do not crucially affect the ID propagation but determine PIDs.

The effect of volume dynamics

The volume of extracellular space (ECS) changes significantly during IDs [36], which affects the discharges [19] and hypothetically might affect the ID propagation. Volume dynamics provide feedback for the modulation of ionic concentrations. A change in ionic balance results in a change in osmolarity and, consequently, volume change, which in turn primarily affects the extracellular concentrations. We describe the volume dynamics with Eq 32, and its effect is considered for the extracellular ion concentrations in Eqs 27–29. The ECS volume is much smaller than the intracellular volume, which is characterized by the ratio β. This ratio is close to the reverse ECS volume fraction estimated from the experiments. The ECS volume fraction ranges from 5% to 36% [37,38]. An effective ECS volume fraction is even less if we exclude the contribution of large reservoirs of ECS into the estimated value, so we set β = 10 in contrast to 7 from the previous modeling study [39]. Since the ECS volume is much smaller than the intracellular volume, any water flux out or inside cells leads to a more significant change of the ECS volume than of the intracellular volume. Therefore, it has a stronger effect on extracellular than intracellular ionic concentrations. The ECS volume reduces after a single ID at almost 50% and gradually recovers between IDs (Fig 6H), which is consistent with the experimental observations [36]. Such a volume change affects the extracellular ionic concentrations even if the intracellular concentrations remain constant. To check the ECS volume change effect on ID generation, we performed a fixed volume simulation (Fig 9F). The simulation shows no significant changes in the frequency and speed of the IDs. The magnitude of modulation of $[K^+]_o$ and other variables during the IDs are almost the same in the simulations with dynamic and

fixed ECS volume, except for the $[Cl^-]_o$ changes, which are bigger in the case of fixed volume. In this case, ID generation is more irregular, observed as a larger difference in interdischarge intervals (compare Fig 9F to 9A).

The effect of glia

To consider the effect of glia, we took into account a glial buffer in the form from [40]. Simulations revealed a quite expected increase of the intervals between IDs but no evident effects on the ID propagation (compare Fig 9I to 9A).

Discussion

The phenomenon of epileptiform discharge propagation

We studied seizure propagation properties using an *in vitro* model of epileptiform activity and mathematical modeling. With electrode recordings made at two distant sites of the cortex, we found an ID propagation speed of less than 0.5 mm/s. In simulations, we reproduced the regime of repeating ID generation and propagation with speed close to the experimental estimates within an order of magnitude. Our experimental observations and simulations are consistent with data in patients and results obtained from *in vivo* and *in vitro* animal models. For instance, Martinet et al. (2015) [41] used invasive subdural electrode arrays covering a broad area of the cortex (8×8 cm) of patients with pharmacoresistant epilepsy to visualize seizure spread and observe waves of cortical region recruitment. They measured a mean recruitment speed of about 4 mm/s. Our estimations (Figs 3B and 4F) are also consistent with the previous EEG and fMRI studies in human patients, where propagation speeds varied from 0.2 to 10 mm/s [42–45]. The multiunit ECoG recordings showed the propagation to be 0.83 mm/s [7]. In *in vitro* models of epileptic activity with the zero magnesium ($0 \, Mg^{2+}$) solutions, the speed varied from 0.1 to 1.34 mm/s [12,46,47].

The speed of the IDs was crucially slower than that of the SDs, including LSDs (referred to as the afterdischarges in other studies [35]) and interictal discharges, which were measured to be > 30 mm/s [2,3,12]. This difference is also evident from our experiments and simulations and corresponds to our previous study on SDs [6]. The ID propagation is much lower than the axonal conduction velocities found in the brain, e.g., for mossy fibers (300 mm/s) [48]. From the other extreme, the ID speed is much faster than that of cortical spreading depression observed in migraine (3 mm/min) [49]. Our simulation with non-spreading connections (Fig 9C) seems to be close to the case of cortical spreading depression. It shows similar speeds of discharges propagating purely by means of potassium diffusion. However, this issue requires further investigation.

Typically, in the late stage of an ID, the LSDs recorded at spatially remote sites are highly correlated [35]. They look synchronized on the time-scale of an entire ID because of their high speed. So, naturally, the IDs recorded at different sites typically cease simultaneously. That is why the ID spread studies reveal the tendency of IDs to be shorter at the locations where the ID front appears later [41], as also seen in our examples.

In our experiments, IDs were preceded by PIDs, which were not seen in the control simulation. However, after consideration of the long-range connections, such PIDs have been revealed in simulations, which clarifies the origin of the discharges: the PIDs were reflected through the long connections from the leading zone of ID generation.

Mechanism of ID generation

The ID origination scenario in our model supports the GABAergic hypothesis of seizure initiation [50,51]. This hypothesis proposes that synchronous activation of inhibitory interneurons underlies the inciting events that result in a seizure. In our case, the involvement of pyramidal cells goes

through chloride accumulation [33,52] rather than through post-inhibitory rebound excitation [51,53]. The synchronous activation of interneurons is also supported by the chloride ion accumulation in these cells. That is why the ionic dynamics play a crucial role in the initiation of ID generation and maintenance of this activity. Therefore, it was essential to describe it in detail in our model. Briefly, intracellular chloride and extracellular potassium ion concentrations elevation provides positive feedback during a single ID generation. In contrast, the intracellular sodium ion accumulation does negative feedback terminating each ID through the activation of the sodium-potassium pump [54]. Considering the fast negative feedback through the short-term synaptic depression and the calcium-dependent potassium channels, we obtain IDs in the form of clustered bursts of spikes. At the peak of depolarization during ID, neurons may show tonic firing or fall into the depolarization block. In total, the scenario is consistent with classical observations [1].

Mechanisms of ictal wavefront propagation

In the literature, several mechanisms of ID and SD propagation were suggested, the first two of which we considered in the present paper (Fig 10): (i) synaptic transmission between neurons, including spike propagation through axons and passive conduction of postsynaptic signals through dendritic neuronal branches [23,24]; (ii) the diffusion of potassium ions, as a substantial transient increase in extracellular potassium ion concentration is observed during IDs [1,22,25,26]; (iii) the ephaptic interactions of neurons through an electric field [55]; and (iv) the electrodiffusion of potassium or glutamate ions in the extracellular space [56].
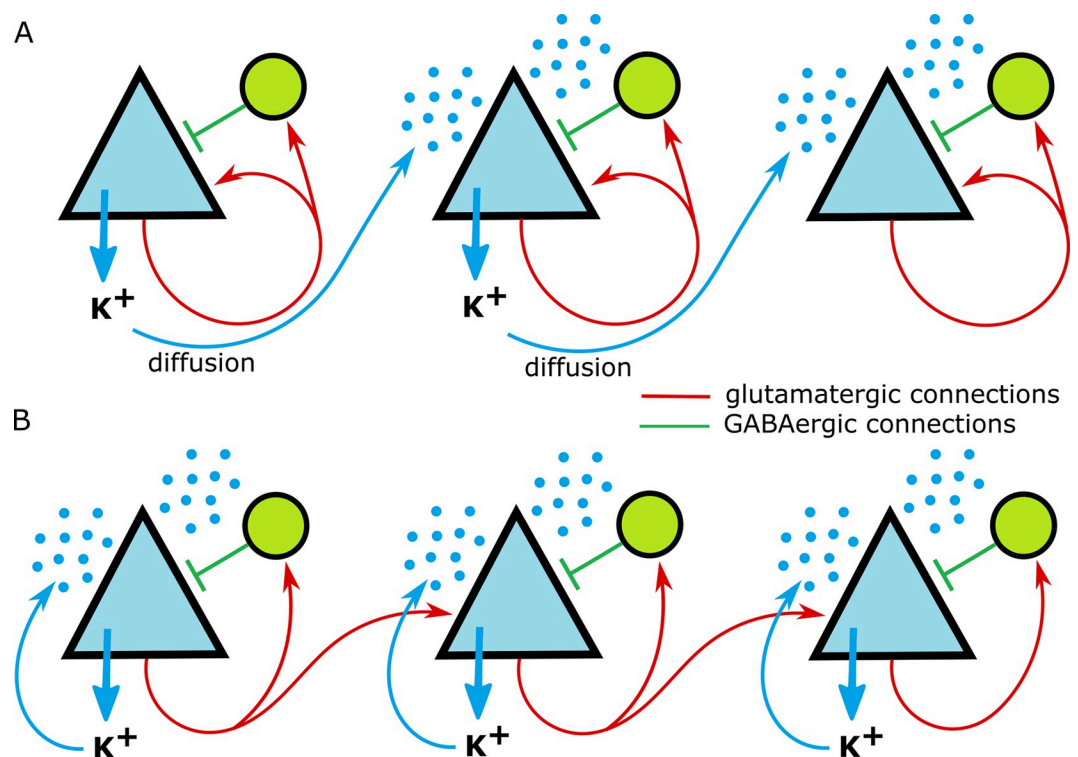
Fig 10. Two alternative mechanisms of ID propagation. (A) The local extrusion and the diffusion in the extracellular space of potassium ions result in potassium ion-mediated depolarization of distant pyramidal cells (blue triangles) and interneurons (green circles). (B) Local extrusion of potassium ions supports excitation of nearby pyramidal cells and interneurons. The pyramidal cells fire their spikes, which propagate through axons and activate glutamatergic receptors, thus providing excitation and extrusion of the potassium ions through voltage-gated and glutamatergic channels, which trigger ID in new locations.

https://doi.org/10.1371/journal.pcbi.1009782.g010

As shown with modeling [6], IID and LSD propagation is determined by neuronal branching and synaptic transmission (the first mechanism) only. However, regarding IDs, with only this fast propagation mechanism being considered, it was unclear how the ictal wavefront travels within cortical tissue at such a slow speed as less than 1 mm/s. Moreover, the wavefront of potassium ion elevation usually accompanies an ID [1], as observed in our experiments. This observation points to the critical role of potassium ion elevation and its depolarizing effect. However, whether the potassium ions spread by diffusion is the cause of the ictal front's propagation (the second mechanism) was an open question. The speed of the potassium ion waves due to ionic diffusion is a constraint made by the effective diffusion coefficient that is affected by the tortuosity and estimated to be less than 1 mm^2/ms [57–59]. It is uncertain if the potassium ion diffusion-based hypothesis and simulations [22] are consistent with the experiments. An artificially increased diffusion coefficient may provide speeds comparable to those of IDs, as in [22], where the coefficient was five orders of magnitude higher than the actual values (1 cm^2/s). Recently, direct evidence concerning the lack of potassium ion diffusion effect on ID propagation from the hippocampus to the neocortex has been provided [60]. The authors reasoned that if activity in the follower territory is triggered by a rise in the number of potassium ions diffused from the other site, then for those events, the rise would appear to occur significantly earlier relative to the local firing. In fact, they have found no significant difference in the latencies, suggesting that the entrainment of neocortical events by the hippocampal activity in their preparation does not happen via the diffusion of potassium ions.

The third mechanism based on ephaptic interactions is known to determine the propagation of slow periodic epileptiform activity in the conditions of absent synaptic interactions [55]. However, it is generally too weak: the extracellular electrical potential with a typical magnitude (about 1 mV) can hardly increase the transmembrane potential up to its threshold value, which is usually much more than a few millivolts above the resting level. Nevertheless, the ephaptic interactions are supposed to trigger excitation in the case of reduced extracellular space [61]. The fourth mechanism of electrodiffusion is also too weak. As estimated earlier [28], the electric field gradients at an order of 2 mV per 100 μm may provide the speed of potassium ions of a few μm/s, which is negligibly small. Therefore, the last two mechanisms can be excluded from consideration. Thus, the present study was aimed to distinguish between the first two mentioned mechanisms of ID propagation through electrophysiological recordings and modeling.

Our simulations have helped to distinguish between the first two mechanisms (Fig 10). We have found that the potassium diffusion-based mechanism (Fig 10A) leads to a much lower speed of propagation, which refutes this hypothesis. On the contrary, the neuronal branching-based mechanism (Fig 10B) determines the ictal front rate; thus, it plays a more important role. In this mechanism, the elevation of $[K^+]_o$ is also essential for the excitation; however, it might be localized, i.e., it follows the propagation of synaptic activity. These findings are consistent with our previous simplified modeling study [28]. We suggest that this mechanism is also the major one that explains the above-mentioned observations made in the *in vitro* models and patients; though, the large-scale recordings with EEG or fMRI electrodes may also reflect the contribution of the cortico-thalamo-cortical loops [41,62–66].

Mechanism of propagation of SDs, which are much faster than IDs

As described in our previous study of SDs with modeling and electrophysiological tools [6], the mechanism of SD propagation includes only synaptic connections. It does not necessitate the ionic dynamics, though the pathologically impaired, quasi-constant level of intracellular chloride ion concentration is required for the generation of SDs. In our present simulations,

the ionic concentrations were dynamic, but the SD mechanism was the same. Thus, it validates the conclusion of our previous study, stating that the SD propagation is independent of the ionic dynamics. In contrast, the ID propagation necessarily involves at least the dynamic change in extracellular potassium ion concentration. Consequently, the ID front propagates much slower than SDs, at the speed of a few tens of mm/s, so on the time scale of an entire ID, SDs are observed as almost synchronous events [2,3].

Factors affecting ID propagation

The present detailed model has revealed the main factors affecting propagation and some of the inefficient ones. The most influential parameter was the length of the connections. In our simulations, it increased the ID speed almost proportionally. It may also explain the bulk difference between the studies in humans and rodents: the typical length of collaterals in human brains is much longer. On the contrary, modulation of the potassium ion diffusion coefficient within its physiological range was inefficient. The volume dynamics and the glial buffering also did not contribute significantly to the ID propagation.

In conclusion, our study distinguishes between two primary hypotheses on the mechanisms of ictal wavefront propagation. It highlights the role of conventional signal propagation through neuronal branches. This axo-dendritic propagation is accompanied by positive feedback excitation provided by the elevation in the level of extracellular potassium ions that are released from excited neurons through voltage-gated and active glutamatergic receptors. These results are of certain importance to novel treatments against epilepsy.

Methods

Ethics statement

Three-week-old male Wistar rats (n = 15) were used in this study. The animals were kept under standard conditions with free access to food and water. All animal procedures followed the guidelines of the European Community Council Directive 86/609/EEC and were approved by the Sechenov Institute of Evolutionary Physiology and Biochemistry Bioethics Committee.

Brain slice preparation

The rats were sacrificed via decapitation, and their brains were removed rapidly. The brain slice preparation method has been described previously (Amakhin et al., 2016; Chizhov et al., 2019). A vibrating microtome (Microm HM 650 V; Microm, Germany) was used to cut horizontal 350-μm-thick slices that contained the hippocampus and the adjacent cortical regions (including the entorhinal cortex (ERC) and the perirhinal cortex (PRC)). Artificial cerebrospinal fluid with the following composition (in mM) was used: 126 NaCl, 24 $NaHCO_3$, 2.5 KCl, 2 $CaCl_2$, 1.25 NaH_2PO_4, 1 $MgSO_4$, and 10 dextrose. The artificial cerebrospinal fluid was aerated with a gas mixture of 95% O_2 and 5% CO_2. All chemicals used to prepare the solutions were purchased from Sigma-Aldrich (St. Louis, MO, USA) unless stated otherwise. 1–2 slices per rat were used for the experiments.

In vitro model of epileptiform activity

Epileptiform activity in rat brain slices was induced using a pro-epileptic solution (Amakhin et al., 2016; Chizhov et al., 2017, 2019), containing the following (in mM): 126 NaCl, 24 $NaHCO_3$, 2.5 KCl, 2 $CaCl_2$, 1.25 NaH_2PO_4, 0.25 $MgSO_4$, 10 dextrose, 0.05 4-aminopyridine. Perfusion of slices with pro-epileptic solution results in an activity similar for ERC and PRC.

Whole-cell patch-clamp recordings

The recordings were performed at 30˚C. Pyramidal neurons in the deep layers of the medial ERC and layer 3 of PRC were visualized using a Zeiss Axioscop 2 microscope (Zeiss, Oberkochen, Germany) equipped with differential interference contrast optics and a video camera (Grasshopper 3 GS3-U3-23S6M-C; FLIR Integrated Imaging Solutions Inc., Wilsonville, OR, USA). Patch electrodes (3–5 MΩ) were pulled from borosilicate glass capillaries (Sutter Instrument, Novato, CA, USA) using a P-1000 pipette puller (Sutter Instrument, Novato, CA, USA). A cesium methanesulfonate-based pipette solution (composition in mM: 127 CsMeSO3, 10 NaCl, 5 EGTA, 10 HEPES, 6 QX314, 4 ATP-Mg, and 0.3 GTP; pH adjusted to 7.25 with CsOH) was used for voltage-clamp recordings. For current-clamp recordings, a potassium gluconate-based pipette solution was used, in mM: 136 K-Gluconate, 10 NaCl, 5 EGTA, 10 HEPES, 4 ATP-Mg, and 0.3 GTP; pH adjusted to 7.25 with KOH. Whole-cell recordings were performed using a Multiclamp 700B (Molecular Devices, Sunnyvale, CA, USA) patch-clamp amplifier and an NI USB-6343 A/D converter (National Instruments, Austin, TX, USA) using WinWCP 5 software (University of Strathclyde, Glasgow, U.K.). The data were filtered at 10 kHz and sampled at 20 kHz. In all cells included in the sample, access resistance was less than 15 MΩ and remained stable ($\leq$20% increase) across the experiment. The liquid junction potential was compensated offline for the voltage-clamp recordings by subtracting 7 mV.

Extracellular potassium ion concentration recordings

Recordings of the extracellular potassium ion concentration were performed using the monopolar K^+-selective microelectrodes [60]. The pipettes were pulled from borosilicate glass (Sutter Instrument). The pipettes' interior surface was exposed to hexamethyldisilazane vapor (Sigma-Aldrich) at 220˚C for 90 min. The pipettes were then backfilled with 100 mM KCl solution. A small volume of the K^+ sensor (Potassium Ionophore I, cocktail A; Sigma-Aldrich, cat. no. 99311) was taken into the salinized pipette's tip using slight suction. The recording of electrode voltage was performed using the Multiclamp 700B patch-clamp amplifier in current-clamp mode. We checked the stability of the electrodes at the start and end of each recording. Data from unstable electrode recordings were discarded. The extracellular K^+ concentration ($[K^+]_o$) at a given moment (t) was calculated from the electrode voltage, (V(t)), as follows:

$$[K^+]_o(t) = 2.5\ e^{S*V(t)},$$

where S is the scaling factor, which was estimated by applying solutions with different $[K^+]_o$ at the tips of ionophore-filled electrodes using a fast application system (HSSE-2/3, ALA Scientific Instruments Inc., USA).

In all electrodes tested, the scaling factor was within a small range (0.043–0.045), so for all obtained recordings, S was set equal to the average value of 0.044mV^{-1}.

Experimental data analysis and statistics

The data analysis was performed using custom software written in Wolfram Mathematica 12 (Wolfram Research, Champaign, IL, USA). To estimate SLE propagation speed, a time lag between the corresponding K^+ transients in ERC and PRC was utilized. The time lag between the $[K^+]_o$ rises was measured at half the peak amplitudes. The characteristic distance was about 2 mm. The upper limit of ID speed propagation was calculated as a ratio of the distance between recorded neurons and the time lag. 2–4 IDs from each slice were recorded for speed estimation.

Sigmaplot 14 (Systat Software Inc., San Jose, CA, USA) was used for the statistical analysis of the results. Dixon's Q-test (at the 95% confidence level) was used to reject outliners. The Kolmogorov–Smirnov test was employed for the evaluation of the normality of sample data. For data that passed the normality test, the results were expressed as mean ± standard error of the mean. Otherwise, the results are expressed as the median and 25%-75% interquartile range (IQR).

A CBRD approach for populations of pyramidal neurons and interneurons

The model for connected populations uses a one-population model as a building block. Such a population receives input signals as synaptic conductances, which are determined by the presynaptic firing rates. The population's output signal is the firing rate, which affects other populations' presynaptic firing rates, as described by the equation of neuronal activity propagation. The population activity is also affected by the gradients of ionic concentrations, determining the ionic channels' driving forces.

The synaptically interacting neuronal populations model is based on our previous study [21]. We consider excitatory and inhibitory neuronal populations, denoted by indices E and I, respectfully, which are distributed in the 1-D space of the x-coordinate and connected by the synaptic AMPA, GABA, and NMDA receptors (Fig 11).

CBRD approach for a single population of neurons

The mathematical description of every single population is based on the probability density approach [67], namely, the CBRD approach [68]. This approach considers a population of an infinite number of Hodgkin–Huxley-like neurons receiving both a common input and an individual noise input for each neuron. In any arbitrary case of transient or steady-state stimulation, such a population's firing rate is approximated with a system of equations in partial derivatives, 1-D transport equations. The equations govern an evolution of neuronal states distributed in the phase space of the time elapsed since the last spike, t^*. The equations include the Hodgkin–Huxley equations for the membrane voltage and gating variables, parameterized by t^*, and the equation for the neuronal density in t^*-space, $\rho^p(t,t^*)$, where the index p substitutes for E or I. The output characteristic of the population's activity is the firing rate $\nu^p(t)$, which is equal to ρ^p in the state of a spike, $t^* = 0$. According to our previous work, the particular form of the equations written below is for regular-spiking pyramidal cells [69,70].
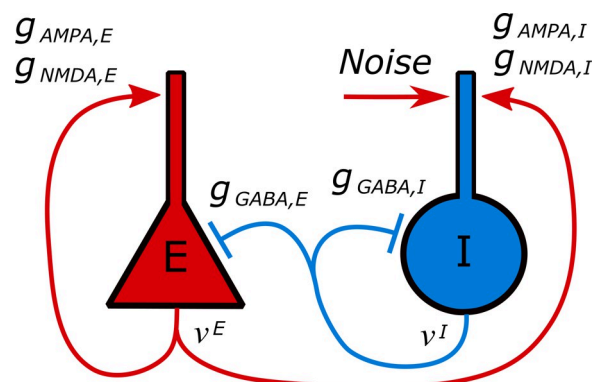

Fig 11. A schematic diagram of the connections between the modeled excitatory and inhibitory populations.

https://doi.org/10.1371/journal.pcbi.1009782.g011

Basic neurons are single-compartment ones with the membrane voltage $U^p(t,t^*)$. Approximations of voltage-gated ionic currents are based on the neocortical pyramidal cell model from [71], including for E-neurons the calcium dynamics and calcium-dependent potassium current that provides an effect of slow spike timing adaptation. Parameterized by t^*, the governing equations are as follows:

$$\frac{\partial \rho^p}{\partial t} + \frac{\partial \rho^p}{\partial t^*} = -\rho^p H(U^p, g_{tot}^p),$$ (1)

$$C\left(\frac{\partial U^p}{\partial t} + \frac{\partial U^p}{\partial t^*}\right) = -g_L(U^p - V_L) - I_{DR} - I_{K-Ca} + I_{noise}$$
$$+ g_{GABA,p}(t)(V_K - U^p) + g_{AMPA,p}(t)(V_{AMPA} - U^p) + g_{NMDA,p}(t)(V_{NMDA} - U^p)$$ (2)

where $g_{tot}^p(t,t^*)$ is the total conductance, including the leak, voltage-gated and synaptic conductance $g_{syn}^p(t, U^p) = g_{AMPA,p}(t) + g_{NMDA,p}(t, U^E) + g_{GABA,p}(t)$.

Hazard function

The source term in the Eq 1 is the hazard function H. This function is defined as the probability to generate a spike for a single neuron that is actually in the state characterized by known neuronal state variables such as the mean membrane potential and gating variables and noise. The approximation of the hazard function H has been obtained for the case of white noise [69] and color noise [70] as a function of $U(t)$ and $g_{tot}^E(t,t^*)$, and parameterized by the noise amplitude in the resting state σ_V^0, the spike threshold voltage V_{th}, and the ratio of the membrane time constant $\tau_m = C/g_{tot}$ to the noise time constant τ_{Noise}, i.e. $k = \tau_m/\tau_{Noise}$:

$$H(U) = A + B,$$ (3)

$$A = \frac{1}{\tau_m} e^{0.0061 - 1.12T - 0.257T^2 - 0.072T^3 - 0.0117T^4} \left(1 - (1 + k)^{-0.71 + 0.0825(T+3)}\right),$$

$$B = \sqrt{2}\left[-\frac{dT}{dt}\right]_+ \sqrt{\frac{2}{\pi}} \frac{\exp(-T^2)}{1 + erf(T)}, \quad T = \frac{V_{th} - U}{\sqrt{2}\,\sigma_V} \sqrt{\frac{g_{tot}^E}{g_L}},$$

where T is the membrane potential relative to the threshold, scaled by the noise amplitude σ_V, which increases with the synaptic conductance: $\sigma_V = \sigma_V^0 \sqrt{1 + g_{syn}/g_L}$. The term A is the hazard for a neuron to cross the threshold because of noise, derived analytically [69] and approximated by exponential and polynomial for convenience; B is the hazard for a neuron to fire because of depolarization due to deterministic drive, i.e., the hazard due to drift in the voltage phase space. Note that the H-function is independent of the basic neuron model and does not contain any free parameters or functions for fitting to any particular case. Thus, H-function is the same for excitatory and inhibitory populations.

Voltage-dependent channels

The set of ionic currents includes the voltage-dependent potassium currents I_{DR} and I_A responsible for spike repolarization, the slow potassium current I_M that contributes to spike frequency adaptation and the potassium current I_{K-Ca}, dependent on calcium dynamics and contributing to slow spike frequency adaptation. Approximating formulas for the currents I_{DR} and I_{K-Ca} are taken from [71].

The voltage-dependent potassium current I_{DR}:

$$I_{DR}(U, t, t^*) = \bar{g}_{DR}n^4(t)(U(t) - V_K), \tag{4}$$

$$\frac{\partial n}{\partial t} + \frac{\partial n}{\partial t^*} = \alpha(U)(1 - n) - \beta(U)n, \tag{5}$$

$$\alpha = -0.032(U + 48)/(\exp(-(U + 48)/5) - 1),$$

$$\beta = 0.5\exp(-(U + 53)/40),$$

The voltage-dependent potassium current I_M:

$$I_M(U, t, t^*) = \bar{g}_{DR}n_M(t)(U(t) - V_K), \tag{6}$$

$$\frac{\partial n}{\partial t} + \frac{\partial n}{\partial t^*} = \alpha(U)(1 - n) - \beta(U)n, \tag{7}$$

$$\alpha = -0.0001(U + 30)/(\exp(-(U + 30)/9) - 1),$$

$$\beta = 0.0001(U + 30)/(\exp((U + 30)/9) - 1),$$

The adaptation current I_{K-Ca}:

$$I_{K-Ca}(U^E, t, t^*) = \bar{g}_{AHP}\, n^2(t)(U(t) - V_K), \tag{8}$$

$$\frac{\partial n}{\partial t} + \frac{\partial n}{\partial t^*} = \alpha(U)[Ca^{2+}]_i^2(1 - n) - \beta(U)n, \tag{9}$$

$$\alpha = 2000mM^{-2}ms^{-1}, \; \beta = 0.002ms^{-1}$$

where $[Ca]_i$ is the intracellular calcium concentration specified below.

Boundary conditions

According to the conservation of the number of neurons in a population, the firing rate is calculated as a sink of neurons from their state t^* due to spiking, $\rho^p(t,t^*)H(U^p(t,t^*))$, integrated over the whole phase space, i.e.

$$v^p(t) \equiv \rho^p(t, 0) = \int_{+0}^{\infty} \rho^p(t,t^*)H(U^p(t,t^*))dt^*. \tag{10}$$

It is the boundary condition for Eq 1.

The spike duration is taken into account by introducing the time interval $0 < t^* < \Delta t_{AP}$ during which the voltage and the gating variables are fixed to their reset values. It defines the boundary conditions for Eqs 2–7 at $t^* = \Delta t_{AP}$ which are as follows:

$$U^E(t, \Delta t_{AP}) = V_{reset} \tag{11}$$

$$I_{DR}: \; n(t, \Delta t_{AP}) = 0.5 \tag{12}$$

The reset values for the fast gating variables in Eqs 10–12 were obtained with the basic single

neuron model. With a rather arbitrary input providing a spike, these values were measured at the moment of a voltage maximum at the spike. The reset level for the slow conductance in the CBRD model was calculated as its value at the peak of spike-release distribution in the t^*-space:

$$I_{K-Ca} : \ n(t, \Delta t_{AP}) = n(t, t^{*p}) \tag{13}$$

where t^{*P} is such that $\rho(t, t^{*p})H(t, t^{*p}) = \max_{0<t^*<+\infty} \rho(t, t^*)H(t, t^*)$.

Parameters

$$\bar{g}_{DR}^E = \bar{g}_{DR}^I = 4 \ \mu S/cm^2,$$

$$\bar{g}_M^E = 0.7 \ \mu S/cm^2, \ \bar{g}_M^I = 0,$$

$$\bar{g}_{K-Ca}^E = 0.4 \ \mu S/cm^2, \ \bar{g}_{K-Ca}^I = 0,$$

$$\tau_m^{0,E} = C/g_{tot}^{0,E} = 28 \ ms, \ \tau_m^{0,I} = C/g_{tot}^{0,I} = 9 \ ms,$$

$$V_{th,0}^E = -50 \ mV, \ V_{th,0}^I = -45 \ mV,$$

$$V_{reset} = -40 \ mV, \ \Delta t_{AP} = 1.5 \ ms,$$

$$C = 1 \ \mu F/cm^2, \ \sigma_V = 3(1 + g_{syn}/g_{tot}^0)mV,$$

$$S = 3 \cdot 10^{-5} \ cm^2$$

$$V_L = -70mV.$$

Here g_{tot}^0 is the total conductance at rest, and g_{syn} is the total synaptic conductance; S is the membrane area; σ_V is the noise amplitude meaning the dispersion of individual neuron's voltage fluctuations in a stationary state. Its scaling with g_{syn} approximately reflects the synaptic noise increase with the increase of mean synaptic drive [72].

The noise term I_{noise} in Eq 2 is nonzero only for the interneurons (Fig 11). It is calculated as an Ornstein-Uhlenbeck process with the amplitude 25pA and the correlation time 4ms.

The depolarisation block is modeled through the dynamic threshold as $V_{th}^{E,I} = V_{th,0}^{E,I} + 100mV \ Sigmoid(U_\infty - V_{DB})/7mV)$, where $Sigmoid(x) = 1/(1+exp(-x))$, $V_{DB} = -40mV$, $\frac{dU_\infty}{dt} = \frac{U(t,t*)-U_\infty}{100ms}$.

When calculating the dynamics of a neural population, the integration of Eqs 2–9 determines the evolution of the distribution of voltage U^E across t^*. Then, the effect of crossing the threshold and the diffusion due to noise are taken into account by H-function, Eq 4, substituted into the equation for neuronal density, Eq 1. The integral Eq 10 results in the output firing rate $\nu^E(t)$.

Connections

The synaptic conductances are described with the second-order differential equations [73] with introduced synaptic plasticity factors $x_{glu}^D(t)$ and $x_{GABA}^D(t)$, i.e. as follows

$$g_{AMPA,j}(t) = \bar{g}_{AMPA,j} m_{AMPA,j}(t) x_{glu}^D(t),$$ (14)

$$g_{NMDA,j}(t, U^j) = \bar{g}_{NMDA,j} f_{NMDA}(U^j(t)) m_{NMDA,j}(t) x_{glu}^D(t),$$ (15)

$$f_{NMDA}(V) = 1/(1 + Mg/3.57\exp(-0.062V)),$$

$$g_{GABA,j}(t) = \bar{g}_{GABA,j} m_{GABA,j}(t) x_{GABA}^D(t),$$ (16)

$$for \quad j = E \; and \; I$$

where Mg is the magnesium (Mg^{2+}) concentration in mM; $m_{s,j}(t)$ is the non-dimensional synaptic conductance which is approximated by the second-order ordinary differential equation:

$$\left(\tau_r^{s,j}\tau_d^{s,j}\frac{d^2}{dt^2} + (\tau_r^{s,j} + \tau_d^{s,j})\frac{d}{dt} + 1\right)m_{s,j}(t) = \tau^{s,j}\left(1 - m_{s,j}(t)\right)\varphi_i(t),$$ (17)

$$\tau^{s,j} = \left(\tau_r^{s,j} - \tau_d^{s,j}\right)/\left(\left(\tau_d^{s,j}/\tau_r^{s,j}\right)^{\tau_d^{s,j}/(\tau_r^{s,j}-\tau_d^{s,j})} - \left(\tau_d^{s,j}/\tau_r^{s,j}\right)^{\tau_r^{s,j}/(\tau_r^{s,j}-\tau_d^{s,j})}\right),$$ (18)

$$if \;\; \tau_r^{s,j} \neq \tau_d^{s,j},$$

$$\tau_r^{s,j}e, \;\; otherwise.$$

Here φ_i is the presynaptic firing rate. In neglect of spatial propagation and temporal delays, the presynaptic firing rate is equivalent to the somatic firing rate, i.e. $\varphi_i \equiv v_i$. The index s is the synapse type, s = AMPA, GABA or NMDA; the index i = E for s = AMPA or NMDA and i = I for s = GABA; w_{glu} and w_{GABA} are the synaptic weights that change because of short-term plasticity; $\bar{g}_{s,j}$ is the maximum conductance, $\tau_r^{s,j}$ and $\tau_d^{s,j}$ are the rise and decay time constants. We imply that the synaptic time constants are estimated from the somatic responses to the stimulation of a presynaptic neuronal population. Thus these time constants characterize not only synaptic channel kinetics but the dendritic and axonal propagation delays as well. The time scale $\tau^{s,j}$ is chosen in the form of Eq 21 in order to provide independence of the maximum of $g_{s,j}(t)$ on $\tau_r^{s,j}$ and $\tau_d^{s,j}$, when $g_{s,j}(t)$ is evoked by a short pulse of $\varphi_j(t)$.

The parameter values were as follows:
$\bar{g}_{NMDA,E} = 0.6 \; mS/cm^2, \bar{g}_{NMDA,I} = 0.9 \; mS/cm^2, \bar{g}_{AMPA,E} = 0.3 \; mS/cm^2, \bar{g}_{AMPA,I} = 0.4 \; mS/cm^2,$ $\bar{g}_{GABA,E} = 1 \; mS/cm^2, \bar{g}_{GABA,I,I} = 2 \; mS/cm^2. \; V_{AMPA} = V_{NMDA} = 0, Mg = 0.25 \; mM, \tau_r^{AMPA,E} = \tau_r^{AMPA,I} = 1.7$ ms, $\tau_d^{AMPA,E} = \tau_d^{AMPA,I} = 8.3$ ms, $\tau_r^{NMDA,E} = \tau_r^{NMDA,I} = 6.7$ ms, $\tau_d^{NMDA,E} = \tau_d^{NMDA,I} = 100$ ms, $\tau_r^{GABA} = 0.5$ ms, $\tau_d^{GABA} = 20$ ms. The GABA reversal potential is determined by the ionic dynamics.

Short-term synaptic plasticity

The synaptic depression was modeled with the Tsodyks-Markram model [74]:

$$\frac{dx_{glu}^D}{dt} = \frac{(1 - x_{glu}^D)}{\tau_{glu}} - U_{glu}\, x_{glu}^D\, \varphi_E(t), \tag{19}$$

$$\frac{dx_{GABA}^D}{dt} = \frac{(1 - x_{GABA}^D)}{\tau_{GABA}} - u_{GABA}\, x_{GABA}^D\, \varphi_I(t), \tag{20}$$

with $\tau_{glu} = \tau_{GABA} = 500$ ms, $u_{glu} = 0.2$, and $u_{GABA} = 0.1$.

A crucial role of short-term synaptic depression in discharge termination was found in experiments and modeling [75]. Simulations with the absence of synaptic depression show that the neuronal populations spontaneously switch to a high-activity state without termination.

Representative neurons

Representative neurons of each of the populations were modeled by the basic single neuron model with the same synaptic inputs as for the populations. This model is described by the equations for the membrane voltage, Eqs 2,3,5–13, where the sum of partial derivatives was substituted by the total derivative in time t, and the sodium current was explicitly present in the right-hand part of Eq 2. The sodium current dependent on voltage V was approximated as in [71]:

$$I_{Na}(t) = \bar{g}_{Na}\, m^3(t) h(t)(V(t) - V_{Na}), \tag{21}$$

$$\frac{dm}{dt} = \alpha_m(U)(1 - m) - \beta_m(U)m, \tag{22}$$

$$\frac{dh}{dt} = \alpha_h(U)(1 - h) - \beta_h(U)h, \tag{23}$$

$$\alpha_m = -0.32(U + 50)/(\exp(-(U + 50)/4) - 1),$$

$$\beta_m = 0.28(U + 23)/(\exp(-(U + 23)/5) - 1),$$

$$\alpha_h = 0.128 \exp(-(U + 46)/18),$$

$$\beta_h = 4/(1 + \exp(-(U + 23)/5)),$$

with $\bar{g}_{Na} = 7\ \mu S/cm^2$ and $V_{Na} = 50 mV$.

Ionic dynamics

The ionic concentrations that strongly affect reversal potentials are the extracellular potassium concentration $[K^+]_o$, the intracellular chloride ion concentrations $[Cl^-]_i^E$ and $[Cl^-]_i^I$ for E- and I-neurons, respectively, and the intracellular sodium concentrations $[Na^+]_i^E$ and $[Na^+]_i^I$ (Fig 12).

The potassium balance equation was modified after Wei et al. [76,77]. The contribution of inhibitory neurons α_I was equal to 1/4 in accordance with the fraction of inhibitory neurons in the cortical tissue. For each of the populations, E and I, the intracellular concentrations of the
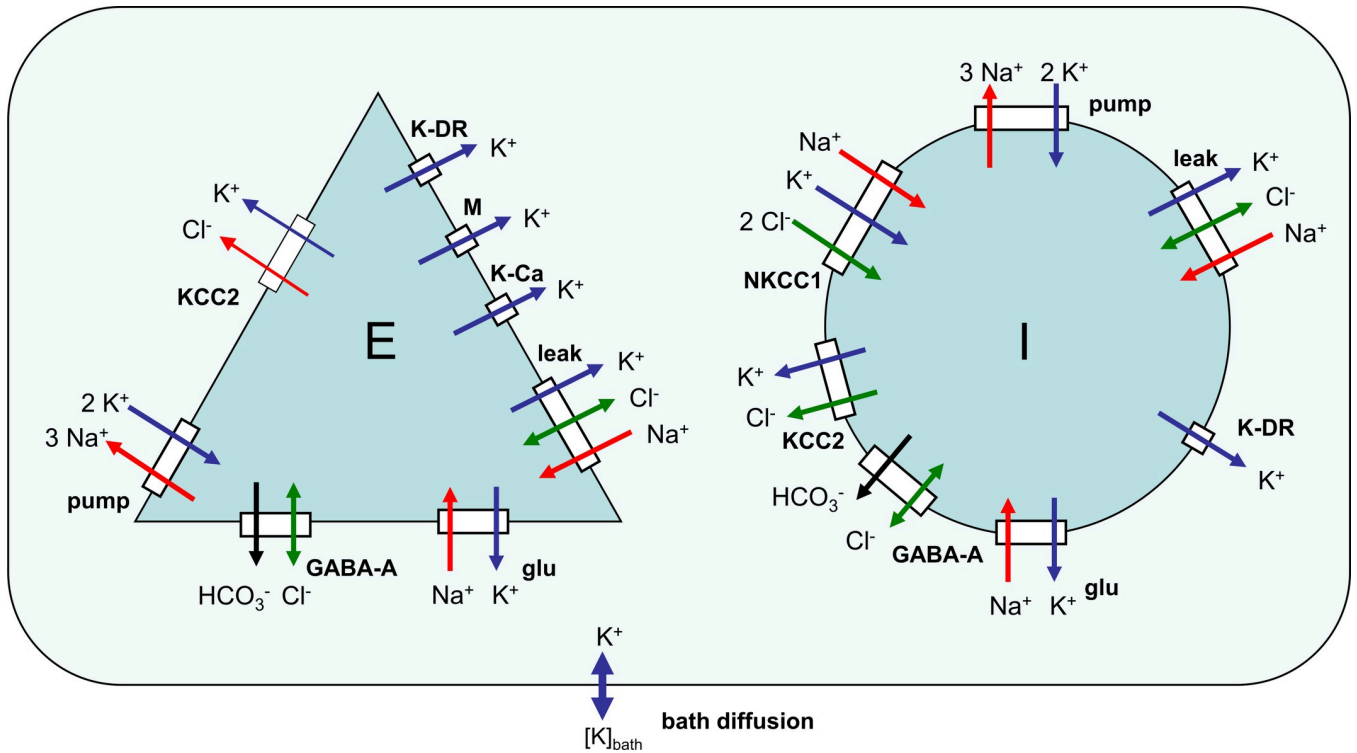
Fig 12. A schematic diagram of ionic dynamics mechanisms. E and I are the populations of pyramidal cells and interneurons. The dynamics of K^+, Cl^-, Na^+, and HCO_3^- ions as determined by the action of the leak, voltage-gated K-DR, A, M, AHP, synaptic $GABA_A$, and glutamatergic channels together with the K^+/Cl^- cotransporters KCC2 and NKCC1 and the Na^+/K^+ exchange pump.

potassium, chloride, and sodium ions were calculated according to the balance equations:

$$\frac{d[K^+]_i}{dt} = \gamma\left[-I_{K,leak} - I_{K,active} - I_{K,glu} + 2I_{pump} + I_{KCC2} + I_{NKCC1}\right] \tag{24}$$

$$\frac{d[Cl^-]_i}{dt} = \gamma\left(I_{Cl,leak} + I_{GABA} + I_{KCC2} + 2I_{NKCC1}\right) \tag{25}$$

$$\frac{d[Na^+]_i}{dt} = \gamma\left(-I_{Na,leak} - I_{Na,glu} + q_{Na}v(t) - 3I_{pump} + I_{NKCC1} + I_{NCX}\right) \tag{26}$$

$$\frac{d(v[K^+]_o)}{dt} = -\beta\left[(1-\alpha_I)\frac{d[K^+]_i^E}{dt} + \alpha_I\frac{d[K^+]_i^I}{dt}\right] + G + D_{bath}\left([K^+]_{bath} - [K^+]_o\right)$$
$$+ D_{1d}\left(\frac{\partial^2[K^+]_o}{\partial x^2}\right) \tag{27}$$

$$\frac{d(v[Cl^-]_o)}{dt} = -\beta\left[(1-\alpha_I)\frac{d[Cl^-]_i^E}{dt} + \alpha_I\frac{d[Cl^-]_i^I}{dt}\right] \tag{28}$$

$$\frac{d(v[Na^+]_o)}{dt} = -\beta\left[(1-\alpha_I)\frac{d[Na^+]_i^E}{dt} + \alpha_I\frac{d[Na^+]_i^I}{dt}\right] \tag{29}$$

where β is the ratio of intra/extracellular volume; $I_{K,leak}^{E/I}$ and $I_{K,active}^{E/I}$ are the potassium currents through the leak and active voltage-gated channels; $I_{K,glu}^{E/I}$ is the potassium current through glutamatergic channels; $I_{pump}^{E/I}$ is the current of potassium dublets, provided by the Na$^+$/K$^+$ pump; $I_{KCC\,2}^{E/I}$ is the flux of potassium due to the KCC2-cotransporter; I_{NKCC1}^{I} is the potassium flux due to the NKCC1-cotransporter taken into account only for the *I*-population; γ is the surface-to-volume and charge-to-concentration translating parameter; $I_{Cl,leak}$ and $I_{Na,leak}$ are the chloride and sodium ion leak currents, respectively; I_{GABA} is the chloride ion current through GABA-A-controlled receptors; and $I_{Na,glu}$ is the sodium current through the glutamatergic receptors. Reversal potentials were obtained from the Nernst equations:

$$V_K = 26.6mV \ln([K^+]_o/[K^+]_i)$$

$$V_{Cl} = 26.6mV \ln([Cl^-]_i/[Cl^-]_o)$$

$$V_{Na} = 26.6mV \ln([Na^+]_o/[Na^+]_i)$$

$$V_{GABA} = 26.6mV \ln((4[Cl^-]_i + [HCO_3^-]_i)/(4[Cl^-]_o + [HCO_3^-]_o))$$

The KCC2 [78] and NKCC1 [77,79] transporter currents were calculated as follows:

$$I_{pump} = \frac{I_{pump,\max}}{(1 + \exp(3.5 - [K^+]_o))(1 + \exp((25 - [Na^+]_i)/3))}$$

$$I_{KCC\,2} = I_{KCC\,2,\max}(V_K - V_{Cl})/(V_K - V_{Cl} - 40\ mV)$$

$$I_{NKCC1} = I_{NKCC1,\max}(V_{Na} + V_K - 2V_{Cl})/26.6\ mV$$

The Na$^+$/K$^+$ pump was taken from [80]:

$$I_{pump}(U, [K^+]_i, [K^+]_o, [Na^+]_i, [Na^+]_o) = I_{pump,max}\frac{\alpha_1^+\alpha_2^+\alpha_3^+\alpha_4^+ + \alpha_1^-\alpha_2^-\alpha_3^-\alpha_4^-}{16.8S_{\alpha\beta}},$$

where $S_{\alpha\beta} = \alpha_1^+\alpha_2^+\alpha_3^+ + \alpha_1^+\alpha_2^+\alpha_4^+ + \alpha_3^+\alpha_2^+\alpha_4^+ + \alpha^{2+}\alpha_3^+\alpha_4^+ + \alpha_1^-\alpha_3^-\alpha_4^- + \alpha_1^-\alpha_2^-\alpha^{4-} + \alpha_2^-\alpha_3^-\alpha_4^- + \alpha_1^-\alpha_2^-\alpha_3^- + \alpha_4^+\alpha_2^+\alpha_1^- + \alpha_4^+\alpha^{2-}\alpha_1^+ + \alpha_4^-\alpha_2^+\alpha_3^+ + \alpha_4^-\alpha_2^+\alpha_3^- + \alpha_1^+\alpha_2^+\alpha_3^- + \alpha_1^+\alpha_2^-\alpha_3^- + \alpha_1^-\alpha_4^-\alpha_3^+ + \alpha_1^-\alpha_3^+\alpha_4^+$; $\alpha_1^- = 8.605$, $\alpha_2^- = \frac{40\ \tilde{Na}_e{}^3}{(1+\tilde{Na}_e)^3+(1+\tilde{K}_e)^2-1}$, $\alpha_3^- = \frac{79300[P]_i[H^+]}{1+Mg\tilde{A}TP}$, $\alpha_4^- = \frac{40\ \tilde{K}_i{}^2}{(1+\tilde{Na}_i)^3+(1+\tilde{K}_i)^2-1}$, $\alpha_1^+ = \frac{1050\ \tilde{Na}_i{}^3}{(1+\tilde{Na}_i)^3+(1+\tilde{K}_i)^2-1}$, $\alpha_2^+ = 481$, $\alpha_3^+ = 2000\frac{\tilde{K}_e{}^2}{(1+\tilde{Na}_e)^3+(1+\tilde{K}_e)^2-1}$, $\alpha_4^+ = \frac{320\ Mg\tilde{A}TP}{1+Mg\tilde{A}TP}$ with $\tilde{Na}_i = \frac{[Na^+]_i}{2.49\ \exp(-0.386U)}$, $\tilde{Na}_e = \frac{[Na^+]_o}{15.5\ \exp(12.1U)}$, $\tilde{K}_i = [K^+]_i/0.5$, $\tilde{K}_e = [K^+]\,o/0.213$, $[H^+] = 1e-4$, $Mg\tilde{A}TP = 3.904$, $[P]_i = 4.2/(1+[K^+]_i/292 + [H^+]/6.77 + [Na^+]_i/224)$, where the concentrations are in mM, the voltage U is in volts here.

Ionic channel currents were calculated based on the membrane potentials averaged across the entire population:

$$\bar{U}(t) = \int_0^\infty U(t,t^*)\rho(t,t^*)dt^*$$

The leak currents are as follows:

$$I_{K,leak} = g_{KL}(\bar{U}(t) - V_K(t)), \ I_{Cl,leak} = g_{ClL}(\bar{U}(t) - V_{Cl}(t)), \ I_{Na,leak} = g_{NaL}(\bar{U}(t) - V_{Na}(t)),$$

$$I_{GABA} = g_{GABA}(t)(\bar{U}(t) - V_{GABA}(t)),$$

$$I_{K,active} = \int_0^\infty (I_{K-DR}(t, t^*) + I_M(t, t^*) + I_{K-Ca}(t, t^*))\rho(t, t^*)dt^*$$

is the average potassium current through the voltage-gated channels. The M- and K-Ca-components are absent for interneurons for simplicity.

The potassium and sodium currents through the glutamatergic channels [81] were approximated as linear dependent on voltage with the fractions of the total glutamatergic conductance. The fraction was estimated as 0.2 for the potassium and 0.4 for the sodium ions [82]:

$$I_{K,glu} = 0.2g_{glu}(\bar{U} - V_K), \ I_{Na,glu} = 0.4g_{glu}(\bar{U} - V_{Na}).$$

The glial buffer is [40]:

$$G = k_1(B_{\max} - B)/k_{1N} - k_2 B, \tag{30}$$

$$\frac{dB}{dt} = k_1(B_{\max} - B) - k_2 B, \ k_2 = k_1/\left(1 + \exp(-([K^+]_o - 15mM)/1.15mM)\right).$$

The **parameters** are as follows:

$\gamma = S/(F\ vol) = 10^{-3}\ [(mM/ms)/(\mu A/cm^2)]; \beta = 10; \alpha_I = 0.25$. The Na$^+$/K$^+$ pump, KCC2, and NKCC1 transporter current amplitudes are as follows: $I_{pump,\max} = 0.8\ \mu A/cm^2$, $I^E_{KCC2,\max} = I^I_{KCC2,\max} = 1\mu A/cm^2, I^E_{NKCC1,\max} = 0, I^I_{NKCC1,\max} = 0.1\mu A/cm^2, [Cl^-]_o = 130\ mM, [K^+]_i = 129\ mM, [Na^+]_o = 130\ mM, [HCO_3^-]_o = 24mM$, and $[HCO_3^-]_i = 16mM$. The leak conductances are the same for both populations: $g_{KL} = 20\ \mu S/cm^2, g_{ClL} = 20\ \mu S/cm^2$, and $g_{NaL} = 7\ \mu S/cm^2$. The membrane area is $3 \cdot 10^{-5} cm^2$. The sodium charge transferred by a single spike is $q_{Na} = 0.1\ \mu C/cm^2$. The potassium concentration mixture with the bath solution was characterized with the parameter $D_{bath} = 0.25s^{-1}$. The coefficient of the spatial diffusion of potassium ions is $D_{1d} = 0.39\ \mu m^2/ms$. The initial concentrations are $[K^+]_o = [K^+]_{bath} = 3.5mM, [Cl^-]^E_i = 5\ mM$, $[Cl^-]^I_i = 9\ mM$, and $[Na^+]^E_i = [Na^+]^I_i = 17\ mM$. The glial pump was neglected in all simulations except the one focused on its effect, where $k_1 = 0.02\ s^{-1}, B_{max} = 500\ mM$.

The calcium concentration inside neurons increases mainly due to the influx through the NMDA receptors and decreases due to the outflow through the sodium-calcium exchangers. The effect of the exchanger is approximated as a relaxation term $I^E_{NCX} = [Ca^{2+}]^E_i/(\gamma\tau_{Ca})$ in the equation for the calcium concentration inside E-neurons

$$\frac{d[Ca^{2+}]^E_i}{dt} = \frac{-[Ca^{2+}]^E_i}{\tau_{Ca}} + \chi g_{NMDA,E}(t)(U^E(t) - V_{Ca}), \tag{31}$$

where the time constant of the relaxation due to Na$^+$/Ca^{2+} exchanger $\tau_{Ca} = 200\ ms$, the contribution of the calcium ions into glutamatergic ionic transport $\chi = 0.001$ and the reversal potential $V_{Ca} = 20mV$. The calcium dynamics was neglected for interneurons.

Volume equation

Extracellular space (ECS) volume dynamics has been described phenomenologically, as in [19]:

$$\frac{dv}{dt} = \frac{1}{\tau_v}\left(1 + 0.1029\beta^0\left(\exp\left(\frac{\Delta\pi}{20}\right) - 1\right) - v\right),\tag{32}$$

where $v = v_o/v_o^0$ is the ratio of the ECS volume to its initial value; $\beta^0 = 10$ is the initial ratio of intracellular versus ECS volumes; $\tau_v = 250\ ms$ is the characteristic time constant of the volume change because of the change of osmolarity $\Delta\pi$:

$\Delta\pi = [Na^+]_i + [Cl^-]_i + [K^+]_i - [Na^+]_o - [Cl^-]_o - [K^+]_o - \Delta\pi^0$, where

$\Delta\pi^0 = [Na^+]_o^0 + [Cl^-]_o^0 + [K^+]_o^0 + [HCO_3^-]_o - [Na^+]_i^0 - [Cl^-]_i^0 - [K^+]_i^0 - [HCO_3^-]_i$.

Equation of neuronal activity propagation

The horizontal cortical connections are supposed to be local and isotropic. They are determined by the relationship between the somatic rates v^i and presynaptic firing rates $\varphi_{i,j}$, where i and j are the indexes of the pre- and postsynaptic populations, respectively. In the case of 1-d geometry, all variables depend on the spatial coordinate x, oriented along with the layers of the cortical tissue. A Gaussian profile of the strengths of the connections is assumed, i.e.

$$\varphi_{i,j}(t,x) = \int v^i(t,x')e^{-(x-x')^2/\lambda^2}dx' \bigg/\!\!\int\!\!\int e^{-(x-x')^2/\lambda^2}dx'\tag{33}$$

where λ is the characteristic length, assumed to be equal for all types of connections, $\lambda = 50$ μm, which roughly corresponds to electrophysiological estimations from paired recordings [83]. In 1-d representation, the cortical area was considered as a segment of the length 2.5mm. The spatial inhomogeneity of parameters was set with the linear distribution of $\bar{g}_{AMPA,E}$, which was equal to zero at $x = 0$, and maximum at $x = L$.

Software and source code

The model was implemented in the software "Brain" that is available from the public repository with DOI: https://doi.org/10.6084/m9.figshare.15113370.v1.

Estimation of activity pattern characteristics

To obtain statistical data from simulations, we varied realizations of the noise term I_{noise} in Eq 2. From 5 realizations of 400s simulations, we used the second, third and fouth IDs, thus obtaining n = 15 values for each characteristic. We estimated the following characteristics of the activity: the speed of the wavefronts, the interdischarge frequency, and the maximum value of the extracellular potassium ion concentration reached during IDs. The first IDs after the onset of the simulation were excluded. For each ID, the speed was estimated from the slope of the slowest fragment of the wavefront, as shown with the black lines in Fig 4B–4D. Similar values were obtained in estimations of a time lag between the K+ transients in remote sites at half the peak amplitudes as indicated in Fig 7A; in this case, the ID speed was calculated as a ratio of the distance between recorded neurons and the time lag. The ID frequency was measured as the reverse time between the fronts at one location S1, so as the maximum extracellular potassium ion concentration. The results are expressed as the median and 25%-75% interquartile range.

Author Contributions

Conceptualization: Anton V. Chizhov, Dmitry V. Amakhin, Elena Yu. Smirnova, Aleksey V. Zaitsev.

Data curation: Dmitry V. Amakhin.

Formal analysis: Anton V. Chizhov, Dmitry V. Amakhin.

Funding acquisition: Anton V. Chizhov.

Investigation: Anton V. Chizhov, Dmitry V. Amakhin, Aleksey V. Zaitsev.

Methodology: Anton V. Chizhov, Dmitry V. Amakhin.

Project administration: Anton V. Chizhov, Aleksey V. Zaitsev.

Software: Anton V. Chizhov.

Supervision: Anton V. Chizhov, Aleksey V. Zaitsev.

Validation: Anton V. Chizhov.

Visualization: Anton V. Chizhov.

Writing – original draft: Anton V. Chizhov, Aleksey V. Zaitsev.

Writing – review & editing: Anton V. Chizhov, Dmitry V. Amakhin, Elena Yu. Smirnova, Aleksey V. Zaitsev.

References

1. Avoli M, D'Antuono M, Louvel J, Köhling R, Biagini G, Pumain R, et al. Network and pharmacological mechanisms leading to epileptiform synchronization in the limbic system *in vitro*. Prog Neurobiol. 2002; 68:167–207. https://doi.org/10.1016/s0301-0082(02)00077-1 PMID: 12450487

2. Ridler T, Matthews P, Phillips KG, Randall AD, Brown JT. Initiation and slow propagation of epileptiform activity from ventral to dorsal medial entorhinal cortex is constrained by an inhibitory gradient. J Physiol. 2018; 596(11):2251–2266. https://doi.org/10.1113/JP275871 PMID: 29604046

3. Trevelyan AJ, Sussillo D, Yuste R. Feedforward inhibition contributes to the control of epileptiform propagation speed. J Neuroscience. 2007; 27(13):3383–3387. https://doi.org/10.1523/JNEUROSCI.0145-07.2007 PMID: 17392454

4. Huberfeld G, de la Prida LM, Pallud J, Cohen I, Le Van Quyen M, Adam C. et al. Glutamatergic pre-ictal discharges emerge at the transition to seizure in human epilepsy. Nature Neuroscience. 2011; 14: 627–634. https://doi.org/10.1038/nn.2790 PMID: 21460834

5. Pallud J, Le Van Quyen M, Bielle F, Pellegrino C, Varlet P, Labussiere M et al. Cortical GABAergic excitation contributes to epileptic activities around human glioma. Science Translational Medicine. 2014; 6:244ra89–244ra89 https://doi.org/10.1126/scitranslmed.3008065 PMID: 25009229

6. Chizhov AV, Amakhin DV, Zaitsev AV. Spatial propagation of interictal discharges along the cortex. Biochemical and Biophysical Research Communications. 2019; 508:1245–1251. https://www.sciencedirect.com/science/article/pii/S0006291X1832713X?via%3Dihub https://doi.org/10.1016/j.bbrc.2018.12.070 PMID: 30563766

7. Schevon CA, Weiss SA, McKhann GJ, Goodman RR, Yuste R, Emerson RG, et al. Evidence of aninhibitory constraint of seizure activity in humans. Nature Communications. 2012; 3:1060. https://doi.org/10.1038/ncomms2056 PMID: 22968706

8. Schevon CA, Tobochnik S, Eiss T, Merricks E, Gill B, Parrish RR, et al. Multiscale recordings reveal the dynamic spatial structure of human seizures. Neurobiology of Disease. 2019; 127:303–311. https://doi.org/10.1016/j.nbd.2019.03.015 PMID: 30898669

9. Smith EH, you Liou J, Davis TS, Merricks EM, Kellis SS, Weiss SA, et al. The ictal wavefront is the spatiotemporal source of discharges during spontaneous human seizures. Nature Communications. 2016; 7(1). https://doi.org/10.1038/ncomms11098 PMID: 27020798

10. Wenzel M, Hamm JP, Peterka DS, Yuste R. Reliable and elastic propagation of cortical seizures *In Vivo*. Cell Reports. 2017; 19(13):2681–2693. https://doi.org/10.1016/j.celrep.2017.05.090 PMID: 28658617

11. Rossi LF, Wykes RC, Kullmann DM, Carandini M. Focal cortical seizures start as standing waves and propagate respecting homotopic connectivity. Nature Communications. 2017; 8:217. https://doi.org/10.1038/s41467-017-00159-6 PMID: 28794407

12. Wong BY, Prince DA. The lateral spread of ictal discharges in neocortical brain slices. Epilepsy Research. 1990; 7(1):29–39. https://doi.org/10.1016/0920-1211(90)90051-v PMID: 1981355

13. Weissinger F, Buchheim K, Siegmund H, Meierkord H. Seizure spread through the life cycle: Optical imaging in combinedbrain slices from immature, adult, and senile rats *in vitro*. Neurobiology of Disease. 2005; 19:84–95. https://doi.org/10.1016/j.nbd.2004.11.013 PMID: 15837564

14. Cammarota M, Losi G, Chiavegato A, Zonta M, Carmignoto G. Fast spiking interneuron control of seizure propagation in a cortical slice model of focal epilepsy. J Physiology. 2013; 591(4):807–822. https://doi.org/10.1113/jphysiol.2012.238154 PMID: 23207591

15. Traub RD, Jefferys JG. Simulations of epileptiform activity in the hippocampal CA3 region in vitro. Hippocampus. 1994; 4:281–285. https://doi.org/10.1002/hipo.450040310 PMID: 7842050

16. Lopes MA, Perani S, Yaakub SN, Richardson MP, Goodfellow M, Terry JR. Revealing epilepsy type using a computational analysis of interictal EEG. Sci Rep. 2019; 9(1):10169. https://doi.org/10.1038/s41598-019-46633-7 PMID: 31308412; PMCID: PMC6629665

17. Arrais M, Modolo J, Mogul D, Wendling F. Design of optimal multi-site brain stimulation protocols via neuro-inspired epilepsy models for abatement of interictal discharges. J Neural Eng. 2020. Epub ahead of print. https://doi.org/10.1088/1741-2552/abd049 PMID: 33271530.

18. Krishnan GP, Bazhenov M, Ionic dynamics mediate spontaneous termination of seizures and postictal depression state. J Neurosci. 2011; 31(24): 8870–8882 https://doi.org/10.1523/JNEUROSCI.6200-10.2011 PMID: 21677171

19. Wei Y, Ullah G, Schiff SJ. Unification of neuronal spikes, seizures, and spreading depression. J Neurosci. 2014; 34(35):11733–11743. https://doi.org/10.1523/JNEUROSCI.0516-14.2014 PMID: 25164668

20. Gentiletti D, Suffczynski P, Gnatkovsky V, de Curtis M. Changes of Ionic Concentrations During Seizure Transitions—A Modeling Study. Int J Neural Syst. 2017; 27(4): 1750004 https://doi.org/10.1142/S0129065717500046 PMID: 27802792

21. Chizhov AV, Amakhin DV, Zaitsev AV. Mathematical model of Na-K-Cl homeostasis in ictal and interictal discharges. PLoS ONE 2019; 14(3):e0213904. https://doi.org/10.1371/journal.pone.0213904 PMID: 30875397

22. Martinet LE, Fiddyment G, Madsen JR, Eskandar EN, Truccolo W, Eden UT, et al. Human seizures couple across spatial scales through travelling wave dynamics. Nature Communications. 2017; 8:14896. https://doi.org/10.1038/ncomms14896 PMID: 28374740

23. Golomb D, Amitai Y. Propagating neuronal discharges trical stimulation above a certain strength. In extracellularin neocortical slices: computational and experimental study. J Neurophysiol. 1997; 78: 1199–1211. https://doi.org/10.1152/jn.1997.78.3.1199 PMID: 9310412

24. Ermentrout B. The Analysis of Synaptically Generated Traveling Waves. J. Comput. Neurosc. 1998; 5: 191–208. https://doi.org/10.1023/a:1008822117809 PMID: 9617667

25. Fertziger AP, Ranck JBJ. Potassium accumulation in interstitial space during epileptiform seizures. Exp Neurol. 1970; 26: 571–585. https://doi.org/10.1016/0014-4886(70)90150-0 PMID: 5435740

26. Durand DM, Park EH, Jensen AL. Potassium diffusive coupling in neural networks. *Philos Trans R Soc Lond B Biol Sci*. 2010; 365(1551):2347–2362. https://doi.org/10.1098/rstb.2010.0050 PMID: 20603356

27. Chizhov AV, Zefirov AV, Amakhin DV, Smirnova EY, Zaitsev AV. Minimal model of interictal and ictal discharges "Epileptor-2". PLoS Comput Biol. 2018; 14(5): e1006186. https://doi.org/10.1371/journal.pcbi.1006186 PMID: 29851959

28. Chizhov AV, Sanin AE. A simple model of epileptic seizure propagation: Potassium diffusion versus axo-dendritic spread. PLoS ONE 15(4): e0230787, 2020. https://doi.org/10.1371/journal.pone.0230787 PMID: 32275724

29. Amakhin DV, Ergina JL, Chizhov AV, Zaitsev AV. Synaptic Conductances during Interictal Discharges in Pyramidal Neurons of Rat Entorhinal Cortex. Front Cell Neurosci. 2016; 10:233. https://doi.org/10.3389/fncel.2016.00233 PMID: 27790093

30. Smirnova EY, Chizhov AV, Zaitsev AV. Presynaptic GABAB receptors underlie the antiepileptic effect of low-frequency electrical stimulation in the 4-aminopyridine model of epilepsy in brain slices of young rats. Brain Stimulation. 2020; 13(5):1387–1395. https://doi.org/10.1016/j.brs.2020.07.013 PMID: 32717394

31. Yelhekar TD, Druzin M, Johansson S. Contribution of Resting Conductance, GABAA-Receptor Mediated Miniature Synaptic Currents and Neurosteroid to Chloride Homeostasis in Central Neurons.

eNeuro. 2017; 4(2): ENEURO.0019-17.2017. https://doi.org/10.1523/ENEURO.0019-17.2017 PMID: 28374007

32. Raimondo JV, Burman RJ, Katz AA, Akerman CJ. Ion dynamics during seizures. Front Cell Neurosci. 2015; 9:419. https://doi.org/10.3389/fncel.2015.00419 PMID: 26539081

33. Burman RJ, Selfe JS, Lee JH, van den Berg M, Calin A, Codadu NK, et al. Excitatory GABAergic signalling is associated with benzodiazepine resistance in status epilepticus. Brain. 2019; 142(11):3482–3501. https://doi.org/10.1093/brain/awz283 PMID: 31553050; PMCID: PMC6904319.

34. Glykys J, Dzhala V, Egawa K, Balena T, Saponjian Y, Kuchibhotla KV et al. Local impermeant anions establish the neuronal chloride concentration. Science. 2014; 343(6171): 670–675. https://doi.org/10.1126/science.1245423 PMID: 24503855

35. Trevelyan AJ, Baldeweg T, van Drongelen W, Yuste R, Whittington M. The Source of Afterdischarge Activity in Neocortical Tonic–Clonic Epilepsy. The Journal of Neuroscience. 2007; 27(49):13513–13519. https://doi.org/10.1523/JNEUROSCI.3005-07.2007 PMID: 18057209

36. Tønnesen J, Inavalli VVGK, Nägerl UV. Super-Resolution Imaging of the Extracellular Space in Living Brain Tissue. Cell. 2018; 172(5):1108–1121. https://doi.org/10.1016/j.cell.2018.02.007 PMID: 29474910

37. McBain CJ, Traynelis SF, Dingledine R. Regional variation of extracellular space in the hippocampus. Science. 1990; 249:674–677. https://doi.org/10.1126/science.2382142 PMID: 2382142

38. Hrabetova S, Cognet L, Rusakov DA and Nägerl UV. Unveiling the Extracellular Space of the Brain: From Super-resolved Microstructure to In Vivo Function. J Neuroscience 2018; 38 (44) 9355–9363; https://doi.org/10.1523/JNEUROSCI.1664-18.2018 PMID: 30381427

39. Somjen GG. Ions in the brain: normal function, seizures, and stoke. Oxford: Oxford University Press; 2004.

40. Bazhenov M, Timofeev I, Steriade M, Sejnowski TJ. Potassium model for slow (2–3Hz) in vivo neocortical paroxysmal oscillations. J Neurophysiol. 2004; 92(2): 1116–1132. https://doi.org/10.1152/jn.00529.2003 PMID: 15056684

41. Martinet LE, Ahmed OJ, Lepage KQ, Cash SS, Kramer MA. Slow Spatial Recruitment of Neocortex during Secondarily Generalized Seizures and Its Relation to Surgical Outcome. J Neurosci. 2015; 35 (25):9477–9490. https://doi.org/10.1523/JNEUROSCI.0049-15.2015 PMID: 26109670

42. Lieb JP, Engel J Jr, Babb TL. Interhemispheric propagation time of human hippocampal seizures. I. Relationship to surgical outcome. Epilepsia. 1986; 27:286–293. https://doi.org/10.1111/j.1528-1157.1986.tb03541.x PMID: 3516670

43. Brekelmans GJF, van Emde Boas W, Velis DN, van Huffelen AC, Debets RMC, van Veelen CWM. Mesial temporal versus neocortical temporal lobe seizures: demonstration of different electroencephalographic spreading patterns by combined use of subdural and intracerebral electrodes. J Epilepsy. 1995; 8:309–320.

44. Blume WT, Ociepa D, Kander V. Frontal lobe seizure propagation: scalp and subdural EEG studies. Epilepsia. 2001; 42:491–503. https://doi.org/10.1046/j.1528-1157.2001.26700.x PMID: 11440344

45. Auer T, Veto K, Doczi T, Komoly S, Juhos V, Janszky J, Schwarcz A. Identifying seizure-onset zone and visualizing seizure spread by fMRI: a case report. Epileptic Disord. 2008; 10:93–100. https://doi.org/10.1684/epd.2008.0187 PMID: 18539559

46. Holtkamp M, Buchheim K, Siegmund H, Meierkord H. Optical imaging reveals reduced seizure spread and propagation velocities in aged rat brain in vitro. Neurobiol Aging. 2003; 24:345–353. https://doi.org/10.1016/s0197-4580(02)00100-8 PMID: 12498969

47. Trevelyan AJ, Sussillo D, Watson BO, Yuste R. Modular propagation of epileptiform activity: evidence for an inhibitory veto in neocortex. J Neurosci. 2006; 26:12447–12455. https://doi.org/10.1523/JNEUROSCI.2787-06.2006 PMID: 17135406

48. Andersen P, Silfvenius H, Sundberg SH, Sveen O, Wigstrom H. Functional characteristics of unmyelinated fibres in the hippocampal cortex. Brain Res. 1978; 144:11–18. https://doi.org/10.1016/0006-8993(78)90431-6 PMID: 638755

49. Eikermann-Haerter K, Ayata C. Cortical spreading depression and migraine. Curr Neurol Neurosci Rep. 2010; 10:167–173. https://doi.org/10.1007/s11910-010-0099-1 PMID: 20425031

50. Avoli M, de Curtis M. GABAergic synchronization in the limbic system and its role in the generation of epileptiform activity. Prog Neurobiol. 2011; 95, 104–132. https://doi.org/10.1016/j.pneurobio.2011.07.003 PMID: 21802488

51. Rich S, Chameh HM, Rafiee M, Ferguson K, Skinner FK and Valiante TA. Inhibitory NetworkBistability Explains Increased Interneuronal Activity Prior to Seizure Onset. Front. Neural Circuits. 2020; 13:81. https://doi.org/10.3389/fncir.2019.00081 PMID: 32009908

52. Lillis KP, Kramer MA, Mertz J, Staley KJ, White JA. Pyramidal cells accumulate chloride at seizure onset. Neurobiol Dis. 2012; 47(3):358–66. https://doi.org/10.1016/j.nbd.2012.05.016 PMID: 22677032

53. Chang M, Dian JA, Dufour S, Wang L, Chameh HM, Ramani M, Valiante TA. Brief activation of GABAergic interneurons initiates the transition to ictal events through post-inhibitory rebound excitation. Neurobiol Dis. 2018; 109, 102–116. https://doi.org/10.1016/j.nbd.2017.10.007 PMID: 29024712

54. Krishnan GP, Filatov G, Shilnikov A, Bazhenov M. Electrogenic properties of the Na/K ATPase control transitions between normal and pathological brain states. J Neurophysiol. 2015; 113: 3356–3374 https://doi.org/10.1152/jn.00460.2014 PMID: 25589588

55. Chiang C-C, Shivacharan RS, Wei X, Gonzalez-Reyes LE, Durand DM. Slow periodic activity in the longitudinal hippocampal slice can self-propagate non-synaptically by a mechanism consistent with ephaptic coupling. J Physiol. 2019; 597(1): 249–269. https://doi.org/10.1113/JP276904 PMID: 30295923

56. Savtchenko LP, Poo MM, Rusakov DA. Electrodiffusion phenomena in neuroscience: a neglected companion. Nature Reviews Neuroscience. 2017; 18: 598–612 https://doi.org/10.1038/nrn.2017.101 PMID: 28924257

57. Vern BA, Schuette WH, Thibault LE. [K+]o clearance in cortex: a new analytical model. J. of Neurophysiology. 1977; 40(5):1015–1023. https://doi.org/10.1152/jn.1977.40.5.1015 PMID: 143510

58. Smith EH, you Liou J, Davis TS, Merricks EM, Kellis SS, Weiss SA, et al. The extracellular space in the CNS: its regulation, volume and geometry in normal and pathological neuronal function. The Neuroscientist. 1997; 3(1):28–41.

59. Chen KC, Nicholson C. Spatial buffering of potassium ions in brain extracellular space. Biophysical journal. 2000; 78(6):2776–2797. https://doi.org/10.1016/S0006-3495(00)76822-6 PMID: 10827962

60. Codadu NK, Parrish RR, Trevelyan AJ. Region-specific differences and areal interactions underlying transitions in epileptiform activity. J Physiol. 2019; 597(7):2079–2096. https://doi.org/10.1113/JP277267 PMID: 30681139

61. Perkins KL, Arranz AM, Yamaguchi Y, and Hrabetova S. Brain extracellular space, hyaluronan, and the prevention of epileptic seizures. Rev Neurosci. 2017; 28(8): 869–892. https://doi.org/10.1515/revneuro-2017-0017 PMID: 28779572

62. Neckelmann D, Amzica F, Steriade M. Spike-wave complexes and fast components of cortically generated seizures. III. Synchronizing mechanisms. J Neurophysiol. 1998; 80:1480–1494. https://doi.org/10.1152/jn.1998.80.3.1480 PMID: 9744953

63. Bertram EH, Mangan PS, Zhang D, Scott CA, Williamson JM. The midline thalamus: alterations and a potential role in limbic epilepsy. Epilepsia. 2001; 42: 967–978. https://doi.org/10.1046/j.1528-1157.2001.042008967.x PMID: 11554881

64. Meeren HK, Pijn JP, Van Luijtelaar EL, Coenen AM, Lopes da Silva FH. Cortical focus drives widespread corticothalamic networks during spontaneous absence seizures in rats. J Neurosci 2002; 22: 1480–1495. https://doi.org/10.1523/JNEUROSCI.22-04-01480.2002 PMID: 11850474

65. Salami M, Itami C, Tsumoto T, Kimura F. Change of conduction velocity by regional myelination yields constant latency irrespective of distance between thalamus and cortex. Proc Natl Acad Sci U S A. 2003; 100:6174–6179. https://doi.org/10.1073/pnas.0937380100 PMID: 12719546

66. Guye M, Régis J, Tamura M, Wendling F, McGonigal A, Chauvel P, Bartolomei F. The role of corticothalamic coupling in human temporal lobe epilepsy. Brain. 2006; 129(7):1917–28. Epub 2006 Jun 7. https://doi.org/10.1093/brain/awl151 PMID: 16760199

67. Gerstner W, Kistler WM, Naud R, Paninski L. Neuronal Dynamics. From Single Neurons to Networks and Models of Cognition. Cambridge University Press; 2014

68. Schwalger T, Chizhov A. Mind the Last Spike—Firing Rate Models for Mesoscopic Populations of Spiking Neurons. Current Opinion in Neurobiology. 58, 155–166, 2019. https://doi.org/10.1016/j.conb.2019.08.003 PMID: 31590003

69. Chizhov AV, Graham LJ. Population model of hippocampal pyramidal neurons linking a refractory density approach to conductance-based neurons. Physical Review E. 2007; 75: 011924. https://doi.org/10.1103/PhysRevE.75.011924 PMID: 17358201

70. Chizhov AV, Graham LJ. Efficient evaluation of neuron populations receiving colored-noise current based on a refractory density method. Physical Review E. 2008; 77: 011910. https://doi.org/10.1103/PhysRevE.77.011910 PMID: 18351879

71. Paré D, Lang EJ, Destexhe A. Inhibitory control of somatodendritic interactions underlying action potentials in neocortical pyramidal neurons in vivo: an intracellular and computational study. Neuroscience. 1998; 84(2):377–402. https://doi.org/10.1016/s0306-4522(97)00530-7 PMID: 9539211

72. Wolfe J, Houweling AR, Brecht M. Sparse and powerful cortical spikes. Curr. Opin. Neurobiol. 2010; 20:306–312. https://doi.org/10.1016/j.conb.2010.03.006 PMID: 20400290

73. Chizhov AV. Conductance-based refractory density model of primary visual cortex. J Comput Neurosci. 2014; 36(2): 297–319. https://doi.org/10.1007/s10827-013-0473-5 PMID: 23888313

74. Loebel A, Tsodyks M. Computation by ensemble synchronization in recurrent networks with synaptic depression. J Comp Neuroscience. 2002; 13: 111–124. https://doi.org/10.1023/a:1020110223441 PMID: 12215725

75. Chizhov AV, Amakhin DV, Zaitsev AV. Computational model of interictal discharges triggered by inter-neurons. PLoS One. 2017; 12(10): e0185752. https://doi.org/10.1371/journal.pone.0185752 PMID: 28977038

76. Barreto E, Cressman JR. Ion concentration dynamics as a mechanism for neuronal bursting. J Biol Phys. 2011; 37(3): 361–373. https://doi.org/10.1007/s10867-010-9212-6 PMID: 22654181

77. Wei Y, Ullah G, Ingram J, Schiff SJ. Oxygen and seizure dynamics: II. Computational modeling. J Neurophysiol. 2014; 112:213–223. https://doi.org/10.1152/jn.00541.2013 PMID: 24671540

78. Doyon N, Prescott SA, Castonguay A, Godin AG, Kroger H, De Koninck Y. Efficacy of Synaptic Inhibition Depends on Multiple, Dynamically Interacting Mechanisms Implicated in Chloride Homeostasis. PLoS Comput Biol. 2011; 7(9): e1002149. https://doi.org/10.1371/journal.pcbi.1002149 PMID: 21931544

79. Ostby I, Oyehaug L, Einevoll GT, Nagelhus EA, Plahte E, Zeuthen T, Lloyd CM, Ottersen OP, Omholt SW. Astrocytin mechanisms explaining neural-activity-induced shrinkage of extracneuronal space. PLoS Comput Biol. 2009; 5:e1000272 https://doi.org/10.1371/journal.pcbi.1000272 PMID: 19165313

80. Smith NP, Crampin EJ. Development of models of active ion transport for whole-cell modelling: Cardiac sodium-potassium pump as a case study. Progress in Biophysics and Molecular Biology. 2004; 85(2–3):387–405. https://doi.org/10.1016/j.pbiomolbio.2004.01.010 PMID: 15142754

81. Rose CR, Konnerth A. NMDA Receptor-Mediated Na1 Signals in Spines and Dendrites. J Neuroscience. 2001; 21(12): 4207–4214.

82. Mayer ML, Westbrook GL. Permeation and block of n-methyl-d-aspartic acid receptor channels by divalent cations in mouse cultured central neurones. J Physiology. 1987; 394: 501–527. https://doi.org/10.1113/jphysiol.1987.sp016883 PMID: 2451020

83. Thomson AM, Lamy C. Functional maps of neocortical local circuitry. Front Neuroscience. 2007; 1:19–42. https://doi.org/10.3389/neuro.01.1.1.002.2007 PMID: 18982117